

Analysis of tropical radiative heating profiles: A comparison of models and observations

Sally A. McFarlane,¹ James H. Mather,¹ and Thomas P. Ackerman^{1,2}

Received 27 November 2006; revised 3 March 2007; accepted 29 May 2007; published 31 July 2007.

[1] The vertical distribution of radiative heating in the atmosphere is an important driver of atmospheric circulation. Evaluation of model simulations of the Earth's radiation budget typically focus only on performance at the top of the atmosphere or at the surface. In this study, we compare the vertical distribution of cloud properties and radiative heating rates calculated from observations at the Department of Energy's Atmospheric Radiation Measurement (ARM) sites on the islands of Nauru and Manus to simulations performed using the Multiscale Modeling Framework (MMF) and the Community Atmosphere Model (CAM). Significant differences are found in the vertical profiles and diurnal cycle of cloud amount, condensed water content, and cloud effect on heating rates between the two models and between the models and the observations. The differences in the heating rates between the models and ARM results depend partly on the details of the parameterization of effective radius and absorption coefficients used and partly on differences in cloud frequency, vertical location of clouds, and optical thickness. Since the same radiative model is used in the CAM and MMF, differences in the effect of clouds on heating rates between the two models are due to the differing treatment of cloud processes in the models and the interaction of clouds and radiation on the local scale in the MMF.

Citation: McFarlane, S. A., J. H. Mather, and T. P. Ackerman (2007), Analysis of tropical radiative heating profiles: A comparison of models and observations, *J. Geophys. Res.*, 112, D14218, doi:10.1029/2006JD008290.

1. Introduction

[2] Radiative heating associated with the distribution of water vapor and clouds in the atmosphere is an important driver of atmospheric circulation, especially in the tropics, and may have important impacts on deep convection and precipitation. In a classic study, *Slingo and Slingo* [1988] showed that removing longwave cloud forcing from a general circulation model (GCM) had a significant impact on tropical circulations. More recently, using a simplified 2-dimensional (2-D) model, *Raymond* [2000] found that cloud-radiation interactions alone were strong enough to drive a Hadley circulation of similar intensity to the observed Hadley circulation. *Zhang and Chou* [1999] found that changes in IR cooling due to water vapor variability affected the rate of generation of convective available potential energy and conditional instability for deep convection. Circulations caused by differences in radiative heating between clear and cloudy regions have been proposed as a mechanism for the diurnal cycle of precipitation [*Gray and Jacobsen*, 1977], although recent

modeling studies have indicated that this differential heating is of secondary importance to the role of the diurnal varying solar radiation in stabilizing the large-scale environment [*Xu and Randall*, 1995; *Tao et al.*, 1996].

[3] Aside from the horizontal variability of water vapor and clouds, radiative heating associated with vertical variability is also important. Dry layers of air are observed frequently in the tropics and the radiative perturbations associated with these layers may affect the development of convection [*Mapes and Zuidema*, 1996]. Persistence of cirrus and stratocumulus layers may be affected by destabilization of the layer due to cloud-base warming and cloud-top cooling [*Lilly*, 1988; *Ackerman et al.*, 1988]. Recently, *Lin et al.* [2004] suggested that the inability of many models to simulate realistic representations of the Madden-Julian Oscillation (MJO) may be caused by systematic diabatic heating profile errors. A recent study by *Hartmann and Larson* [2002] has emphasized the role of radiative heating in possible climate system feedback. Using a radiative-convective equilibrium model they illustrate that the air temperature at which the clear-sky cooling rate begins to decrease stays roughly constant with increasing sea surface temperature. They then assume that radiatively-driven convergence and hence anvil cloud tops will occur at approximately the same temperature, even in a warmer climate. To examine such effects in global models, it is necessary that model clouds be able to respond realistically to changes in large-scale forcing. Models must produce cloud and radiative heating rate profiles with realistic horizontal,

¹Climate Physics Group, Pacific Northwest National Laboratory, Richland, Washington, USA.

²Joint Institute for the Study of the Atmosphere and Ocean and Department of Atmospheric Sciences, University of Washington, Seattle, Washington, USA.

vertical, and diurnal variability in order to produce realistic tropical circulations and cloud feedbacks.

[4] One of the difficulties in producing accurate cloud and heating rate profiles within a large-scale general circulation model (GCM) is the sub-grid scale nature of cloud dynamical processes and their interactions with radiation. Within a GCM, cloud processes are generally treated with parameterizations which contain parameters whose values are derived from observations or higher resolution models or are adjusted so that simulations resemble observations. The outputs of GCM cloud parameterizations are generally gridbox mean values of cloud fraction and cloud condensate. Vertical structure is prescribed using simple overlap assumptions. In reality, clouds exhibit significant horizontal variability and vertical structure on the scales of a GCM gridbox. A new approach to climate modeling, the multi-scale modeling framework (MMF), reduces (although does not eliminate) the need for cloud parameterizations by coupling cloud-scale dynamics with the larger scale dynamics of the GCM. The MMF, also known as the cloud-resolving convection parameterization [Grabowski, 2001] or super-parameterization [Khairoutdinov and Randall, 2001; Randall et al., 2003; Khairoutdinov et al., 2005] treats cloud processes more explicitly by replacing the cloud and radiation parameterizations of a GCM with a 2-D cloud system resolving model (CSRM) embedded in each GCM gridbox. The CSRM explicitly resolves cloud dynamics and physical processes down to the resolution of the CSRM. Radiative transfer calculations are run directly on each CSRM column, removing the need for any assumptions of cloud overlap, however cloud microphysical processes are still parameterized within the CSRM. The CSRM is forced by the large scale tendencies from the GCM and returns the average of the cloud and radiative tendencies over the CSRM columns back to the GCM.

[5] Due to the non-linear nature of radiative transfer as a function of optical depth, the average radiation calculated from a distribution of cloud properties is not the same as the radiation calculated from the average cloud properties [Cahalan et al., 1994]. The inclusion of sub-grid scale variability of clouds and radiation in the MMF framework may significantly impact the simulated climate. A recent study by Cole et al. [2005] found that cloud-radiation interactions at scales unresolved by GCMs were at least as important as accurate domain averages of radiative fluxes. Analysis of MMF simulations is ongoing, but several studies have indicated that the MMF produces better defined MJO-like systems, a more realistic diurnal cycle of precipitation over land, and more realistic frequency distribution of precipitation in the tropics [Randall et al., 2003; Khairoutdinov et al., 2005; Ovtchinnikov et al., 2005]. In this study, we investigate how the sub-grid scale treatment of clouds in the MMF affects the vertical distributions of cloud properties and radiative heating.

[6] Although the vertical re-distribution of energy by clouds has important feedbacks to model dynamics, evaluation of model simulations of the Earth's radiation budget typically focus on performance at the top of the atmosphere (TOA) or the surface [Kiehl et al., 1998], neglecting details of the distribution of radiation within the vertical column. Evaluation of vertical profiles of model fluxes or heating rates is difficult because of the lack of direct observations of

heating rate profiles in the atmosphere. Current estimates of cloudy sky radiative heating in the tropics are based primarily on model simulations (e.g., Fu et al. [1995]), satellite observations with limited vertical resolution [Bergman and Hendon, 1998; Zhang et al., 2004], or observations during short field programs [Cox and Griffith, 1979]. The long time series of observations taken at the Department of Energy's Atmospheric Radiation Measurement (ARM) program sites on the islands of Manus and Nauru in the tropical Pacific provides a unique dataset for calculating all-sky heating rate profiles with high vertical and temporal resolution in the tropics. In a previous study, Mather et al. [2007], we used the ARM observations to derive cloud properties and calculate radiative heating rates for non-precipitating clouds over several months at both Nauru and Manus. In this study, we combine those cloud and heating rate profiles with observations of the surface energy budget to evaluate the simulated vertical profiles of cloud properties and radiative heating produced by the MMF and the Community Atmosphere Model (CAM) 3.0 models. Section 2 describes the observations and calculated heating rate profiles while section 3 describes the details of the model simulations. Section 4 presents comparisons of the cloud and heating rate profiles calculated from the ARM observations and simulated by the models while section 5 discusses the conclusions of this study.

2. Observations and Calculated Heating Rate Profiles

[7] We use observations taken at the ARM sites on the island republic of Nauru (0.52° S, 166.92° E) and at Manus, Papua New Guinea (2.06° S, 147.40° E) in the tropical western pacific (TWP) to determine the energy budget at the surface as well as the vertical profiles of cloud properties and heating rates. The ARM sites have been operating on Manus since 1996 and on Nauru since 1998 and contain a suite of ground-based active and passive remote sensors [Mather et al., 1998]. Radiosondes are launched twice a day under normal conditions. The time series of broadband shortwave (SW) and longwave (LW) radiation measurements at the two sites are almost continuous since their installation. Due to the complexity of the active sensors and the harsh operating conditions at these remote tropical sites, the time series of vertically profiling measurements is more limited. In this study, we examine the radiation measurements and cloud property and heating rate profiles from February to July 2000 at Manus and March to December 1999 at Nauru.

[8] Manus is located in the core of the tropical warm pool, a region of high convective activity, while Nauru is located at the eastern edge of the warm pool and experiences large interannual variability in convective activity associated with the El Nino/Southern oscillation (ENSO) cycle. During El Nino, convection tends to shift eastward, leading to more active convection at Nauru. The period of March-December, 1999 is a period of suppressed conditions at Nauru, with little active convection. Manus experiences a wide range of seasonal and interannual variability associated with the Madden-Julian Oscillation as well as its location near the Maritime Continent [Mather, 2005].

[9] Details of the retrieved cloud properties and heating rate calculations are given in *Mather et al.* [2007]. Vertical profiles of condensed water content (CWC) and particle size for non-precipitating clouds are retrieved from the millimeter wavelength cloud radar (MMCR) and microwave radiometer (MWR) measurements with 10 second temporal and 45 meter vertical resolution. Vertical profiles of temperature and water vapor are derived by combining radiosonde profiles with higher temporal resolution measurements of total water vapor from the MWR and surface air temperature. The resulting cloud microphysical and atmospheric state profiles are sampled every 5 minutes and broadband fluxes and vertical heating rate profiles are calculated using a correlated-k distribution radiative transfer model [*Fu and Liou*, 1992]. The parameterization of cloud optical properties follows *Fu et al.* [1995] for liquid clouds and *Fu* [1996] and *Fu et al.* [1998] for ice clouds. Ozone profiles and temperature and humidity profiles above 100 mb are based on a standard tropical atmosphere. Aerosol is neglected in the heating rate calculations, but is assumed to be relatively low at these tropical oceanic sites [*Smirnov et al.*, 2002].

[10] Downwelling broadband SW and LW radiation at the surface is measured by a suite of radiometers. Clear sky periods are determined from the downwelling shortwave radiation measurements following the procedure of *Long and Ackerman*, [2000]. A simple 2-parameter function of solar zenith angle is fit to the measured clear-sky irradiances and used to infer clear-sky irradiance values during periods of cloudy sky. A similar procedure is performed to infer clear-sky LW fluxes [*Long*, 2004]. Observed all-sky fluxes and inferred clear-sky fluxes are averaged to daily values. The difference (all-sky – clear-sky) is used to determine the effect of clouds on the surface radiative budget.

3. Details of Model Simulations

[11] The details of the MMF configuration are given by *Khairoutdinov and Randall* [2001] and *Khairoutdinov et al.* [2005]. The MMF consists of a parent GCM with an individual CSRM running in each GCM grid column. The CSRM replaces the subgrid-scale cloud and radiation parameterizations of the parent model. In the version of the MMF being run at Pacific Northwest National Laboratory and used in this study, the parent GCM is the NCAR Community Atmosphere Model (CAM 3.0), which is the atmospheric component of the Community Climate System Model (CCSM) [*Blackmon and Coauthors*, 2001]. The CAM is run with the finite volume dynamical core and has 26 vertical layers and horizontal resolution of 2° latitude and 2.5° longitude. The dynamical time step of the CAM is 20 minutes and the radiation time step is 1 hour.

[12] Details of the CAM physics can be found in *Collins et al.* [2004]. Stratiform cloudiness, deep convection, and shallow convection are all treated with separate parameterizations. Total cloud condensate is a prognostic variable, and separation of total condensate into liquid and ice depends solely on temperature. Precipitation is also diagnosed as rain or graupel-like snow. Cloud fraction is diagnosed as a function of relative humidity, atmospheric stability, and convective mass flux. Three types of cloud fraction are diagnosed: low-level marine stratus, convective

cloud, and layered cloud. Total cloud fraction at each level is the maximum of the individual cloud fractions in the level. Optical properties of liquid clouds [*Slingo*, 1989] and ice clouds [*Ebert and Curry*, 1992] are parameterized. The calculation of SW radiation uses the δ -Eddington approximation, as described in *Briegleb* [1992]. Longwave radiative transfer is based on an absorptivity/emissivity formulation using a broad band model approach described in *Kiehl and Briegleb* [1991]. The CAM 3.0 uses the new cloud overlap parameterization of *Collins* [2001] which is designed to reproduce calculations based on the independent column approximation.

[13] The embedded CSRM [*Khairoutdinov and Randall*, 2001] within each CAM grid cell has 64 columns at 4 km spacing and 24 layers in the vertical, which coincide with the lowest 24 levels of the CAM. The CSRM domain is aligned in the east-west direction with cyclic lateral boundary conditions. The CSRM runs continuously with its own 20-second dynamical timestep. Radiation calculations using the CAM radiative transfer code are performed on each CSRM column every 10 minutes, using the time averaged temperature, water vapor and cloud fields from the CSRM. The CSRM is forced by the large-scale tendencies from the CAM every CAM time-step and the horizontally averaged heating and moisture fields from the CSRM are fed back to the CAM as the tendencies due to subgrid-scale processes. Each of the CSRM columns has the same surface conditions, which are imposed by the CAM land surface model; no column represents a particular location within the gridbox.

[14] The CSRM predicts liquid water and ice moist static energy (which is the sum of the sensible, potential, and latent heat energy), total non-precipitating water (vapor + liquid + ice) and total precipitating water (rain + snow + graupel). Partitioning of cloud condensate and precipitating water is done every time step as a function of temperature then the resulting mixing ratios are used to compute the sedimentation and hydrometeor conversion rates [*Khairoutdinov and Randall*, 2001]. The CSRM uses the same optical property parameterizations and radiation code as the CAM, although no overlap approximation is needed as each CSRM grid box is either clear or cloudy, with no fractional cloud cover.

[15] The MMF simulation was initialized on 1 September 1997 using initial model fields from a CAM spinup simulation and was run through 2001, using observed monthly sea surface temperatures (SST). A CAM model run was performed for the same period with the same SST values. For comparisons with the observations, the output from the CAM gridbox nearest the ARM sites is used. For the MMF, the 64 CSRM columns within the nearest GCM gridbox to the ARM sites are used.

4. Results

[16] Comparisons of time series of observations at a point to model grid box averages are difficult because of the inherent differences in the spatial and temporal scales of the models and the observations [*Jakob et al.*, 2004]. Some of these difficulties are ameliorated in this study by only examining long-term averages and frequency distributions. Additionally, the MMF serves as a link between the fine temporal and spatial scale of the observations and the large

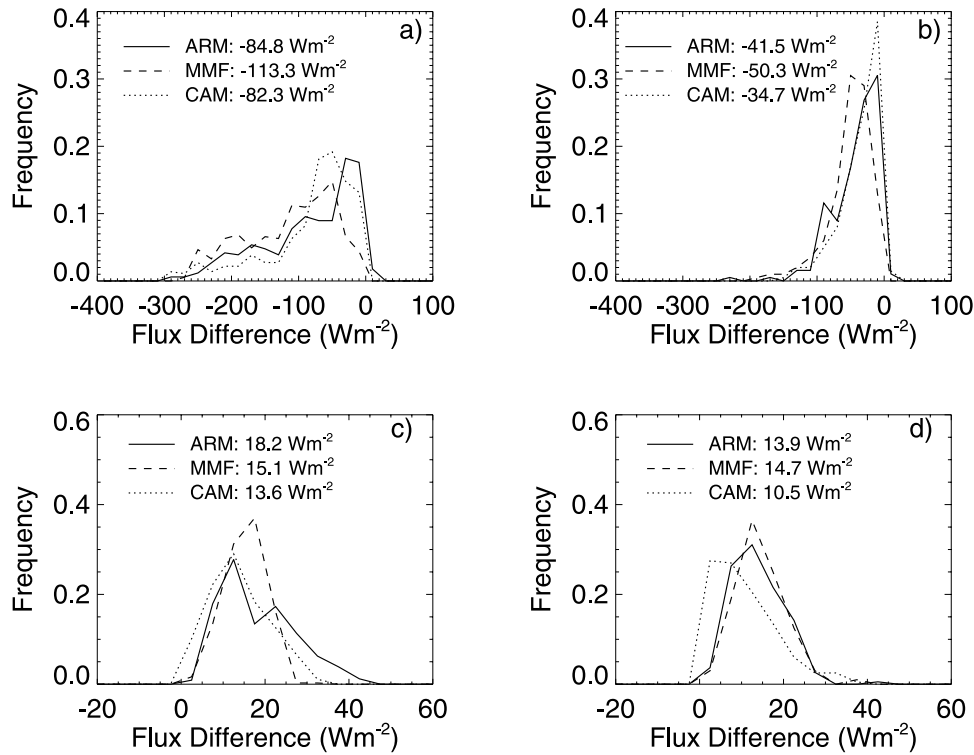


Figure 1. Frequency distributions of cloud effect (all-sky minus clear-sky) on surface (a) SW flux at Manus, (b) SW flux at Nauru, (c) LW flux at Manus, (d) LW flux at Nauru for the ARM measurements (solid lines), MMF model (dashed line) and CAM model (dotted line). The mean surface cloud effect for each dataset is given in the legend.

scale GCM. Time series or frequency distributions of CSRM column quantities can be compared more directly to the observed surface time series, while the MMF gridbox averages can be compared more directly to the CAM values and the satellite observations.

[17] Evaluation of GCM simulations of the Earth's radiation balance typically focus on performance at the TOA or the surface. Here, we briefly examine the ability of the models to simulate the daily average surface cloud effect, which we define as all-sky flux minus clear-sky flux. Histograms of the cloud effect at the surface over the study periods at the two sites (Figure 1) show that the CAM produces reasonable estimates of the effect of clouds on both the SW and LW radiation at the surface. The MMF significantly overestimates the SW cloud effect at Manus but agrees with the observations as well as the CAM at Nauru and is in reasonable agreement with the LW cloud effect at both sites. The MMF overestimates the average SW cloud effect at Manus due to underestimation of the frequency of clear sky (small SW flux differences) and overestimation of the frequency of optically thick clouds with strong SW cloud effects (SW flux differences between -100 and -300 Wm^{-2}) at Manus. The MMF is in reasonable agreement with the average measured LW cloud effect at Manus, but underestimates the variability. The same surface radiation can be produced by a number of different cloud vertical profiles and errors in the correct specification of the vertical distribution of cloud properties may compensate to produce reasonable values at the bound-

aries. In the remainder of this section, we examine the differences in the vertical distributions of clouds and radiative heating rates in the ARM dataset and model simulations.

4.1. Vertical Distribution of Clouds at Manus

4.1.1. Cloud Frequency

[18] The column energy budget and the distribution of radiative heating within the column depend on total cloud amount, optical properties of cloud layers, and the vertical distribution of clouds [Stephens and Webster, 1981]. The vertical distribution of non-precipitating cloud frequency from the ARM observations at Manus shows a trimodal structure (Figure 2). Peaks in cloud frequency occur near 1 km, 5 km and 12–13 km. The peak near 5 km is associated with a weak stable layer that occurs near the melting level [Johnson *et al.*, 1999]. Observed clouds with tops at this altitude are generally cumulus congestus or thin altocumulus layers. The peak at 1 km is associated with shallow boundary layer clouds and the broad peak from 8 to 13 km represents ice clouds associated with anvil outflow from deep convection. The observations show a minimum in cloud between 2 and 4 km as seen in other studies [Zuidema, 1998]. Cloud is rarely observed above 15 km in the radar dataset.

[19] The vertical distributions of mean cloud frequency from the MMF and average gridbox cloud fraction from the CAM are similar in shape to the ARM distribution of cloud frequency, but differences in the location and magnitude of peak cloudiness are apparent (Figure 2). The MMF results

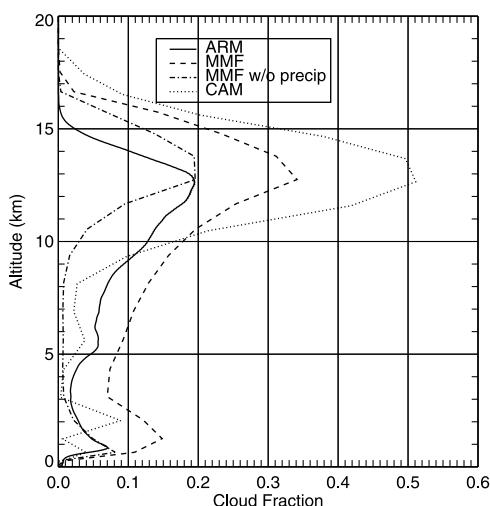


Figure 2. Vertical distribution of average cloud frequency at Manus from ARM observations (solid line), average cloud frequency from individual CSRM columns in the MMF simulation (dashed line), average cloud frequency from the MMF simulation with precipitating columns removed (dashed-dotted line), and average gridbox cloud fraction from the CAM simulation (dotted line). Model gridboxes are defined to be cloudy if in-cloud condensed water $>10^{-4} \text{ gm}^{-3}$ and radar range gates are defined to contain cloud if reflectivity $>-60 \text{ dBZ}$.

do not show a distinct peak in cloud frequency at the freezing level, although they have a high frequency of clouds between 4 and 10 km. The MMF boundary layer cloud feature is more frequent, occurs at higher altitudes, and is broader than the ARM boundary layer feature. The MMF ice cloud feature is also more frequent and there is significant cloud frequency up to 16 km. The CAM has a bi-modal boundary layer cloud feature, with one peak at similar altitude to the ARM boundary layer feature and one peak significantly higher. The peak frequency of ice clouds in the CAM occurs at a similar altitude as the observations, but the cloud fraction is significantly higher than the ARM frequency of occurrence and the CAM has ice cloud up to 18 km.

[20] The radiative effect of clouds in the CAM is a combination of both the cloud fraction and the cloud condensed water content. The CAM cloud fraction is diagnosed as a function of relative humidity and atmospheric stability (for layered clouds) or as a function of convective mass flux (for convective clouds). In the 3-hour output files, information on the components (layered and convective) of the total cloud fraction was retained. The frequency distribution of total gridbox cloud fraction and convective cloud fraction from the 3-hour output files for all clouds produced in the CAM is shown in Figures 3a, 3b. The CAM column is rarely completely clear; shallow convection is almost always occurring in the model. Convective cloud has gridbox cloud fraction of $<40\%$ at all levels. Low-level layer cloud occurs near 2 km, with cloud fraction ranging up to 70%. Cirrus layers occur frequently from 10 to 15 km with a strong peak at 100% cloud cover and frequent cirrus cloud with cloud fraction less than 20% occurs above 15 km. The CAM can have large values of cloud fraction with

vanishingly small values of in-cloud CWC. Figures 3c, 3d show the same frequency distributions, but gridboxes with in-cloud CWC less than 10^{-4} gm^{-3} (which roughly corresponds to the detection limit of the cloud radar) are set to zero cloud fraction. It is evident that the convective parameterization produces frequent occurrence of cloud throughout the lower troposphere, but significant amounts of condensed water detrain at only 3 distinct levels in the lower troposphere: near the melting level at 5 km, near 3 km, and near 1 km, resulting in the bimodal boundary layer cloud fraction seen in the previous figure.

[21] 85% of the CAM clouds which contain ice have cloud top heights greater than 15 km at Manus, compared to 29% of the MMF ice clouds and 6% of the ARM ice clouds. A previous comparison of lidar and radar cloud detection at the Nauru site [Comstock *et al.*, 2002] indicated that the radar routinely misses cloud top heights above 15 km that are detected by the lidar (45% of lidar detected cirrus) and the radar missed all cirrus with cloud bases above 15 km (13% of the lidar detected cirrus). The radar has reduced sensitivity to these upper tropospheric clouds because they tend to be optically thin and contain small ice crystals, which have small microwave backscattering cross sections. Comparison of the optical depth frequency distributions from Figure 3 in Comstock *et al.* [2002] suggests that the cirrus not detected by the radar has optical depth less than 0.1. Similar sensitivity of the radar is expected at the Nauru and Manus sites. The ARM radar observations obviously underestimate the frequency of cirrus clouds with tops greater than 15 km at Manus. The CAM has a significantly larger frequency of cirrus with high cloud tops than observed in the Comstock *et al.* [2002] study and it seems likely that the CAM overestimates the frequency of these high clouds. Previous studies have indicated that the CAM has too much high level cloud compared to satellite observations [Lin and Zhang, 2004]. It is unclear from this analysis if the MMF is under- or over-estimating the frequency of high clouds at Manus.

[22] As discussed in Mather *et al.* [2007], precipitating columns were removed from the observational dataset because there are no suitable algorithms for retrieving cloud properties during precipitation. Surface rain gauge measurements and a reflectivity threshold were used to identify profiles containing precipitation, which resulted in 13% of the Manus radar data being removed from the observational dataset. The absence of precipitating clouds in the observational dataset may be one reason for differences between the observed and model vertical distributions of cloud frequency. In the MMF simulations, information on precipitation was retained in the output files. When MMF columns which have surface precipitation rate greater than 0.1 mm/hr or which contain layers with precipitating rain water content greater than 10^{-4} gm^{-3} are removed (33% of columns), the magnitude of the peaks in ice cloud and boundary layer cloud frequency are much more similar to the ARM observations (Figure 2). The boundary layer cloud feature is also narrowed considerably, indicating that many of the deeper boundary layer clouds were precipitating. The new MMF profile has virtually no cloud occurrence between 3 and 10 km, indicating that all mid-level cloud in the MMF is associated with precipitation. In the CAM simulations, statistics on precipitation were not retained in the 1-hour

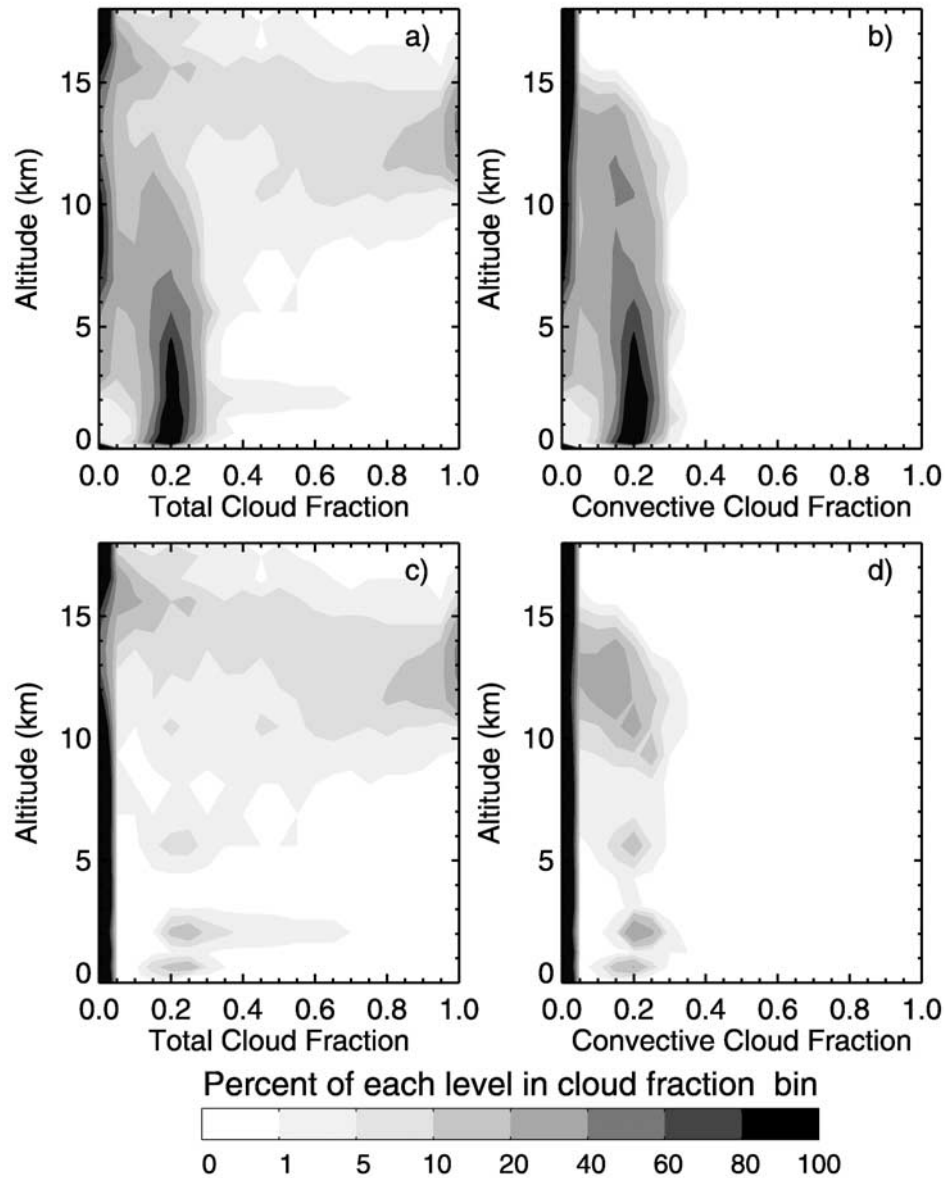


Figure 3. Frequency distribution of (a) gridbox total cloud fraction, (b) gridbox convective cloud fraction, (c) gridbox total cloud fraction for gridboxes with in-cloud CWC $>10^{-4} \text{ gm}^{-3}$, (d) gridbox convective cloud fraction for gridboxes with in-cloud CWC $>10^{-4} \text{ gm}^{-3}$ from the CAM at Manus. Frequency distributions are normalized so that sum of each level is 100 percent.

output files, so precipitating columns could not be removed. Previous studies indicate that the frequency of convection in the CAM leads to an unrealistic precipitation distribution, with a very high frequency of light precipitation events [Ovtchinnikov *et al.*, 2005; Zhang and Mu, 2005], so little cloud would remain if precipitating columns were removed.

4.1.2. Microphysical Properties

[23] The impact of clouds on the radiation budget depends not only on their spatial distribution, but also on their microphysical properties. Figure 4 shows frequency distributions of in-cloud condensed water content (CWC) retrieved from the ARM observations, and from the MMF and CAM models. In the MMF profile, the region with

CWC less than 10^{-3} gm^{-3} from 4 to 12 km is associated with the treatment of ice sedimentation in the MMF. The sedimentation routine used in this study (which has been corrected in newer versions of the model) resulted in a layer of very small condensate amount being deposited just below cloud base. Sensitivity tests indicated that the small CWC amounts in the sediment region have only a small impact on the calculated heating rate profiles. We convert the CAM grid-box average CWC to in-cloud CWC (by dividing by the cloud fraction) for better comparison with other results. The in-cloud CWC is weighted by the cloud fraction in the calculation of the frequency distribution. The median grid-box average CWC is also shown in Figure 4. From 0 to

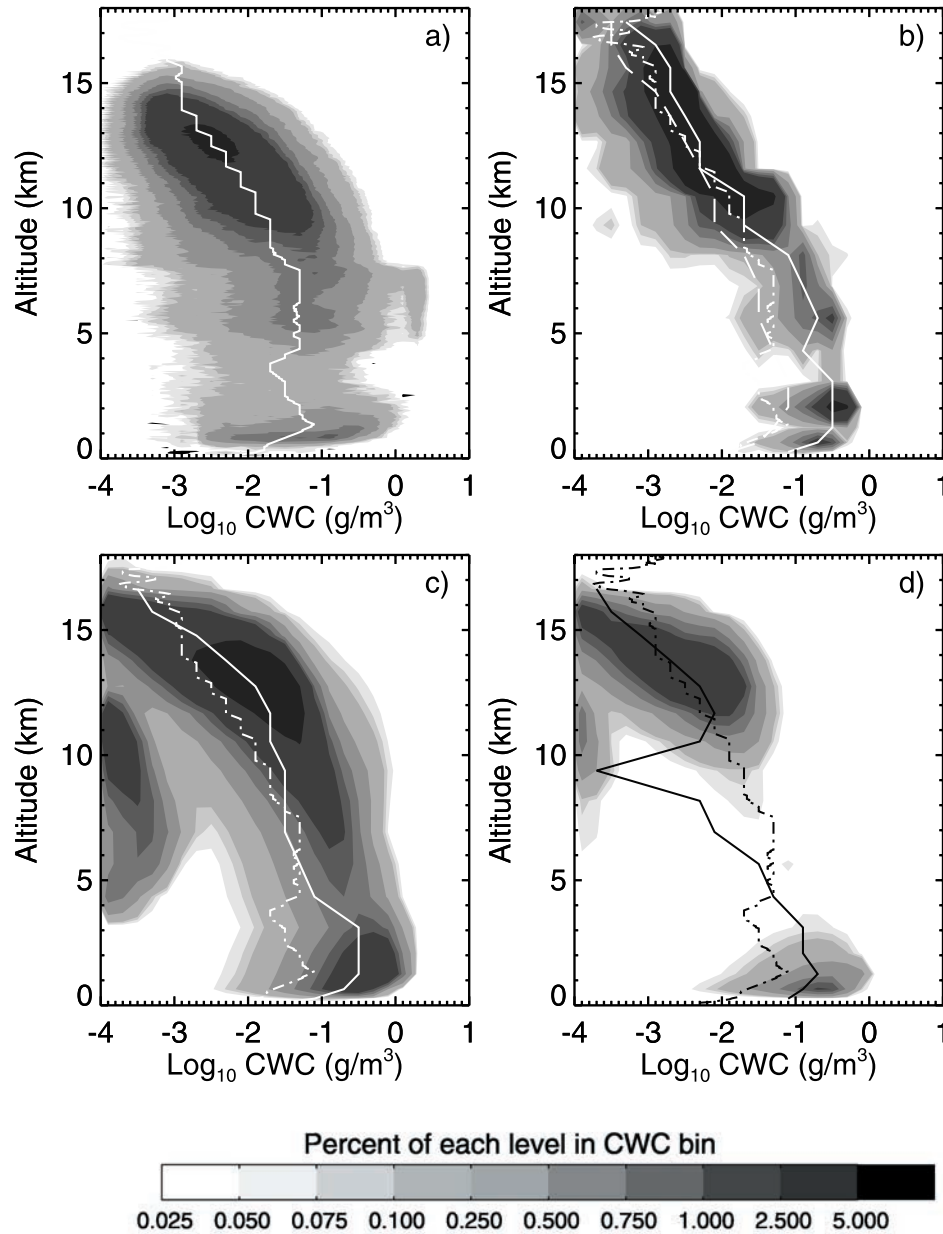


Figure 4. Frequency distributions of in-cloud CWC at Manus from (a) ARM retrievals, (b) CAM model, (c) MMF model, (d) MMF model with precipitating columns removed. The shading represents the percentage of radar retrievals or model gridboxes at each level that fall within the given CWC bin. The frequency distributions are normalized such that the sum of each level is 100%. Clear layers are included in the normalization although not shown in the plot. The median CWC of the cloudy points at each level is also indicated by the solid lines. The dashed line in (b) represents the median of the grid-box average CWC in the CAM. The ARM median CWC is also plotted as a dashed-dotted line on each frequency distribution for comparison purposes.

10 km and 15 to 18 km, which are regions with low cloud fractions, the CAM median in-cloud CWC is significantly greater than the median grid-box average CWC; from 10 to 18 km, which has higher cloud fractions, the values are more similar.

[24] The observations and models have a similar range of CWC in the boundary layer clouds, although the models have larger median values. The CAM has a double peak in boundary layer CWC, which was also seen in the

average cloud fraction (Figure 2, 3). The MMF dataset has a larger median CWC value in the ice cloud layer than the other datasets. Both the MMF and ARM datasets have a wide range of ice water content (IWC), with maximum IWC an order of magnitude larger than seen in the CAM. The CAM has a narrow range of CWC at all levels due to the lack of sub-grid scale variability and has an abrupt transition in CWC near 9 km due to the different

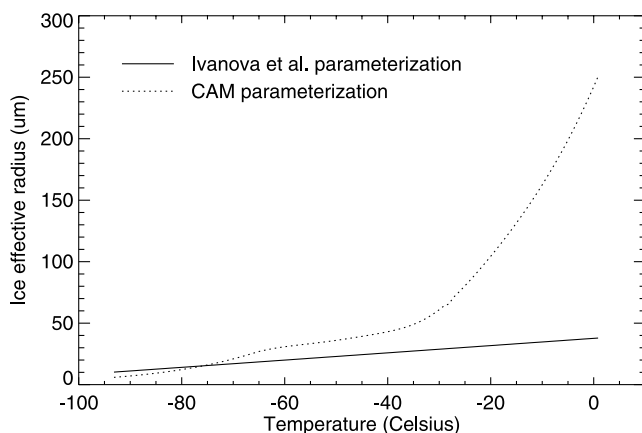


Figure 5. Parameterizations of ice effective radius as a function of temperature. *Ivanova et al.* [2001] parameterization (solid line) is used in ARM retrievals and CAM parameterization (dotted line), which is based on Kristjánsson et al. [2000], is used in CAM and MMF simulations.

treatment of cloud condensate in the convective and stratiform parameterizations.

[25] The radiative effect of clouds also depends on their particle size. In both the models and the ARM retrievals, ice cloud effective radius is determined as a function of temperature. For the ARM retrievals, ice cloud effective radius is calculated from the parameterization of *Ivanova et al.* [2001], while the parameterization in the CAM/MMF radiative transfer code is based on the work of *Kristjánsson et al.* [2000]. In general, the CAM parameterization gives a significantly larger effective radius for a given temperature than the ARM retrieval (Figure 5). The radiation codes used in the CAM/MMF and in the ARM calculations also have different parameterizations of mass absorption coefficient as a function of particle size. Ice absorption in the longwave decreases with increasing particle size, so we would expect the CAM and MMF to have smaller infrared absorption coefficients since they have larger particle sizes. However, the CAM/MMF parameterization (which is based on a modification of *Ebert and Curry* [1992] and is independent of wavelength) has a larger absorption coefficient than the *Fu et al.* [1998] parameterization for all particle sizes and wavelengths (Figure 6). In this comparison, the differences in absorption coefficient and particle size between the model and ARM calculations act in opposite directions and partially cancel; if the datasets had used the same temperature parameterization but different parameterization of absorption coefficients, the differences would be magnified. These large differences in the particle size and infrared ice absorption parameterizations show the difficulty in examining the radiative effects of ice clouds and the importance of the radiative parameterizations used. The SW parameterizations of ice optical properties used in the CAM and MMF calculations [*Ebert and Curry*, 1992] and the ARM calculations [*Fu and Liou*, 1993] agree more closely than the LW parameterizations. For liquid clouds, the optical properties are based on Mie calculations in both radiation codes. However the effective radii of liquid clouds are quite different between the models and ARM retrievals.

In the CAM and MMF, liquid cloud effective radius is parameterized to be $14.0 \mu\text{m}$ for ocean sites. The liquid effective radius retrieved from the ARM observations varies with time, but is often smaller than the model values. The mean value at 850 m (peak of liquid cloud fraction) at Manus is $5.2 \mu\text{m}$.

[26] The probability density functions (pdf) of broadband visible in-cloud optical depth for liquid and ice clouds are shown in Figure 7. For liquid clouds, the CAM optical depth pdf is as broad as the ARM pdf, but shifted toward lower optical depth values. For ice clouds the CAM has a much narrower range of optical depth than the ARM or MMF results. The MMF ice cloud pdf peaks at higher values of optical depth than the ARM results. When precipitating columns are removed from the MMF, the liquid optical depth pdf shifts to significantly lower values while the ice optical depth pdf shows a much smaller change. The peak in very low optical depth values in the MMF is due to the problem with the sedimentation routine discussed previously. The ice cloud infrared optical depth pdfs (Figure 7c) have similar shapes as the visible optical depth pdfs, but smaller values. The narrow peak of the CAM optical depth distribution is a function both of the narrow range of CWC and of the narrow range of ice cloud physical thickness (Figure 8) in the CAM.

[27] Contributions to total ice optical depth can come from cirrus cloud (defined as ice cloud with minimum base ≥ 8 km) or from mid-level clouds (defined as clouds containing ice with bases between 4 and 8 km). In the ARM observations mid-level clouds have very different distributions of physical thickness than cirrus clouds (Figure 8). ARM non-precipitating mid-level clouds have a bimodal distribution of physical thickness, either fairly shallow (< 2 km) or fairly deep (> 5 km), while most cirrus clouds have physical thickness less than 5 km. The MMF mid-level cloud distribution has an increased frequency of very thin clouds and a peak at cloud thickness > 9 km that is associated with precipitating clouds. The CAM shows little difference in the physical thickness or optical thickness of cirrus and mid-level clouds (Figure 7d). The ARM cirrus clouds have lower optical depths and a reduced frequency of $\tau > 1$ relative to the mid-level clouds,

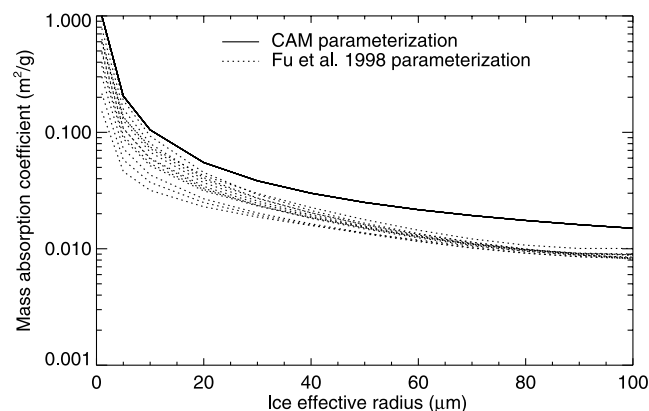


Figure 6. Parameterization of ice infrared mass absorption coefficient in CAM parameterization (solid line) and for each infrared band in *Fu et al.* [1998] parameterization (dotted lines).

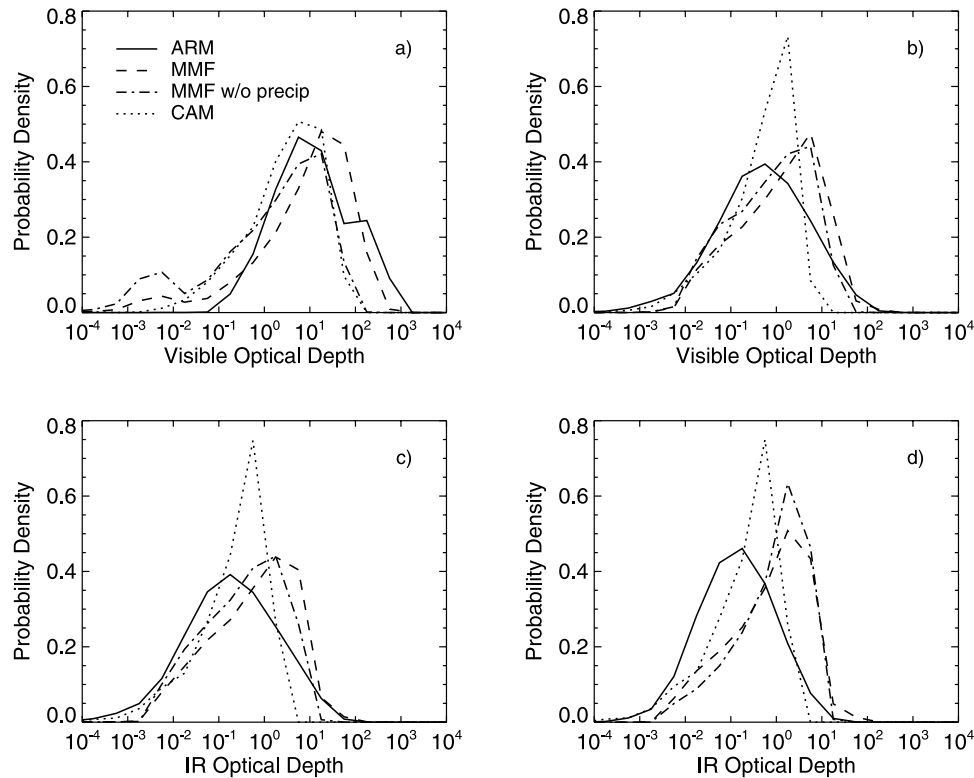


Figure 7. Probability density of (a) broadband visible liquid optical depth, (b) broadband visible ice optical depth, and (c) infrared ice optical depth for all cloudy columns in each Manus dataset and (d) infrared ice optical depth for columns containing only cirrus (lowest cloud base >8 km) in each Manus dataset. For the CAM and MMF, infrared ice optical depth does not vary with wavelength. For the ARM calculations, the infrared optical depth in the $1100\text{--}980\text{ cm}^{-1}$ band is plotted. The probability densities are calculated using bin widths of 0.2 in \log_{10} of optical depth.

indicating that the optically thickest ARM clouds have bases <8 km. The MMF cirrus distribution has a reduced frequency of clouds with $\tau < 1$; mid-level clouds in the MMF are primarily optically thin.

4.2. Heating Rate Profiles at Manus

[28] Specification of the correct vertical distribution of cloud properties is important to climate simulation because clouds redistribute energy vertically within the atmospheric column and this energy distribution affects local and large-scale dynamics. In this section we examine the vertical distribution of heating and cooling within the clear-sky atmosphere as well as the average effect of clouds on the vertical heating rate profiles.

[29] Profiles of both all-sky and clear-sky heating rates are needed so that the impact of clouds on the average heating rate profile can be determined. Unfortunately, the clear-sky heating rate profiles from the model simulations were not saved. Because of the computational expense of re-running the MMF simulation, all-sky and clear-sky heating rates were calculated from the model cloud distributions using an off-line version of the CAM radiation model. The off-line radiation computations were kept as close as possible to the original radiation calculations in the models, but aerosol was neglected since appropriate parameters were not saved in the output files. As in the original calculations, heating rates for the MMF simulations were calculated

every 10 minutes, using the average temperature, water vapor, and cloud properties. For the CAM simulations, heating rates were calculated every 60 minutes, using the temperature, water vapor, and cloud properties calculated at that timestep. The diurnal variation of solar radiation was included in the offline calculations by using the solar zenith angle at the middle of the given time step. Comparison of the average all-sky heating rate profiles calculated with the off-line model to the average profiles from the interactive model simulations found maximum differences in heating rates of 0.16 K/day for the MMF and 0.26 K/day for the CAM in the ice cloud layer. Differences in the rest of the column were much lower, and the shapes of the profiles were not significantly different between the original and off-line calculations (not shown).

4.2.1. Clear Sky Heating Rate Profiles

[30] The structures of the clear-sky heating rates calculated from the observations and models are broadly similar but have some important differences (Figure 9). The average clear-sky heating rate profiles show strong LW cooling at the surface and LW cooling throughout much of the troposphere, with a local maximum near 8 km. The decrease in LW cooling rate above 10 km is due primarily to the decrease in saturation water vapor pressure with decreasing temperature that reduces water vapor emission [Hartmann *et al.*, 2001]. The shortwave (SW) average clear-sky heating rate profiles show heating throughout the troposphere due to

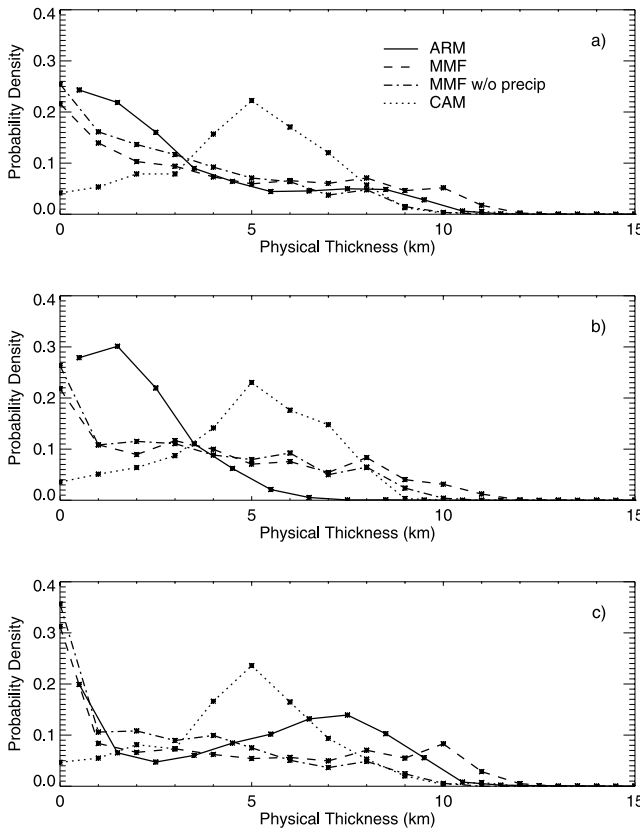


Figure 8. Probability density of ice cloud physical thickness in Manus datasets for (a) all ice clouds, (b) cirrus ice clouds (bases >8 km) and (c) mid-level ice clouds (clouds containing ice and with bases between 4–8 km). Physical thickness is defined as difference between maximum and minimum heights at which $\text{CWC} > 10^{-4} \text{ gm}^{-3}$ and $\text{IWC} > 0 \text{ gm}^{-3}$. If the cloud is actually multi-layer, the physical thickness will be overestimated. For the CAM and MMF distributions, probability densities were calculated using a bin width of 1 model level and model levels were converted to altitude using an average pressure profile. For the ARM distribution, a bin width of 1.0 km was chosen to give roughly the same number of height bins as in the models.

absorption by water vapor, with a maximum heating around 5–6 km and then a decrease with altitude. SW heating increases again in the stratosphere due to ozone absorption. The average net heating rate profile has cooling throughout the troposphere, but transitions to net heating near the tropopause. The clear-sky net radiative cooling in the troposphere leads to the large-scale background subsidence in the tropics [Hartmann and Larson, 2002]. The height at which net radiative heating equals zero (Q_0) is an important component of the radiation balance in the tropopause transition layer and may play a role in troposphere-stratosphere exchange [Hartmann et al., 2001; Gettelman et al., 2004]. The level of clear-sky Q_0 is near 15 km in all three profiles.

[31] The ARM clear-sky heating rate profiles show much stronger LW cooling at the surface than the model heating rates, due primarily to diurnal heating of the land surface at

the ARM site on Manus. The model gridbox which includes the Manus site is primarily ocean-covered and has lower surface temperatures and less variability between surface temperature and air temperature than a land site. The CAM LW clear-sky profiles show a double cooling peak in the mid-troposphere, which is not seen in the ARM or MMF results. The CAM SW profile also has minima near 4 km and 8 km. These differences in the CAM clear-sky heating rate profiles are caused by differences in the water vapor profiles. The average water vapor profile for the MMF and the ARM site are similar in magnitude and both show a smooth exponential decrease with altitude (Figure 10). The MMF has larger average water vapor mixing ratio from 10 to 15 km, which is the cause of the slightly stronger cooling in the MMF profiles at this altitude. The CAM average water vapor mixing ratio profile has several deviations from a smoothly decaying profile, which occur at the same heights as the dips in the clear-sky heating rate profiles. These structures in the CAM average water vapor profiles are a result of the moist convective adjustment procedure used in the CAM shallow and middle-level convective parameterization in which temperature and humidity profiles are adjusted back to neutral, saturated profiles whenever they tend to become unstable and saturated [Collins, 2001]. Since the CSRM within the MMF explicitly predicts moist static energy and water vapor mixing ratio, convective adjustment is not needed.

4.2.2. Effect of Clouds on Heating Rates

[32] Differences between the all-sky heating rate profiles (Figure 11) and the clear-sky heating rate profiles are examined to isolate the effects of clouds on the heating rate profiles (Figure 12). The average effect of boundary layer clouds is to produce (relative to clear-sky) SW cooling below the cloud layer, LW warming below and at the base of the cloud layer, and LW cooling at the top of the cloud layer. The heights of these features vary slightly among the profiles due to the differences in the boundary layer cloud heights in the observations and model simulations (Figure 2). SW cooling below the low cloud layer is caused by the reflection of solar radiation from the clouds, which reduces the amount of radiation available for water vapor absorption. Within the middle troposphere, the average effect of clouds is slight LW warming (due to absorption of radiation emitted by higher clouds) and slight SW cooling (due to reflection of SW by higher clouds). Absorption by cloud particles causes strong LW and SW warming within the ice cloud layer. The largest average LW warming is near the base of the ice cloud layer because it is influenced by absorption of radiation from the ground and the atmosphere below the cloud, while the SW heating peaks higher in the layer.

[33] There are large differences in the effect of ice clouds on the vertical heating rate profiles in the model and ARM results (Figure 12). These differences are due both to differences in cloud amount and vertical location, and to differences in the optical depth distributions. All datasets show strong SW heating in the ice cloud layer. The peak SW heating corresponds roughly to the peak in cloud amount, which is lower in the ARM dataset. The MMF has the largest SW heating peak because of the large ice cloud optical depths and high frequency of ice clouds. When precipitating columns are removed from the MMF,

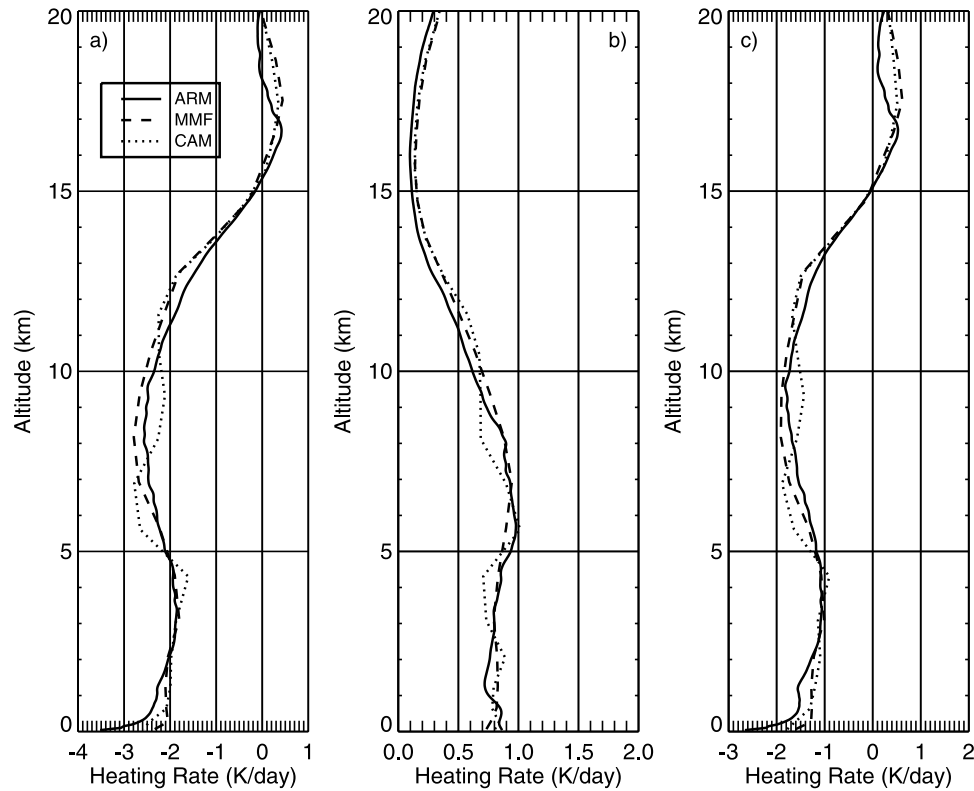


Figure 9. Average (a) longwave, (b) shortwave, and (c) net clear-sky heating rate profiles at Manus calculated from ARM observations (solid line), MMF simulation (dashed line), and CAM simulation (dotted line).

the average ice optical depth and the ice cloud frequency decrease, but there are still a large number of high optical depth clouds. The CAM has similar magnitude of peak SW heating to the ARM results despite the lower optical depths because of the much larger frequency of ice clouds in the CAM than in the ARM results. Additionally, the CAM and MMF have significantly larger ice particles than the ARM retrievals and SW absorption increases with increasing particle size [Ebert and Curry, 1992].

[34] The effect of ice clouds on the longwave is more complicated because ice clouds can both heat (near cloud base in optically thick clouds or throughout cloud depth in optically thin clouds) and cool (near cloud top in optically thick clouds) a layer. When the effects of LW heating and cooling are examined separately all datasets show regions of both heating and cooling due to ice clouds above 8 km (Figure 13). The MMF has the strongest LW heating, due to high cloud frequency and large optical depth values. The LW heating due to clouds in the CAM extends up to 17 km due to the high frequency of optically thin ice clouds. Although the MMF also has ice clouds extending up to 17 km, it has little LW heating above 14 km. The clouds that extend up to 17 km in the MMF are frequently optically thick ice clouds, which have LW cooling at cloud top. The magnitude of the peak ARM longwave heating is considerably less than the MMF or the CAM. The ARM dataset has a much lower frequency of ice cloud than the CAM and has lower frequency of optically thick ice clouds than the MMF. The ARM results also show a lower magnitude of peak heating because the location of ice cloud base is more

variable than in the model results. The ARM results have significant LW heating and cooling between 5 and 8 km due to mid-level clouds, which often contain some ice [Mather *et al.*, 2007]. The amount of heating in an upper level cloud also depends on the temperature of the radiating surface below. There will be less heating at the base of an upper level cloud if there is a mid-level cloud (cold surface) than if

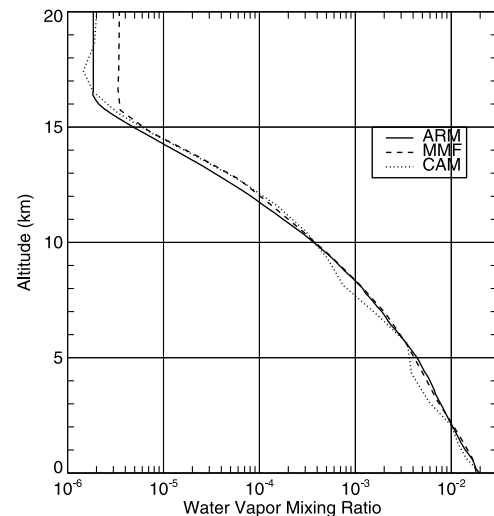


Figure 10. Average profiles of water vapor mixing ratio at Manus from ARM observations (solid line), MMF simulation (dashed line), and CAM simulation (dotted line).

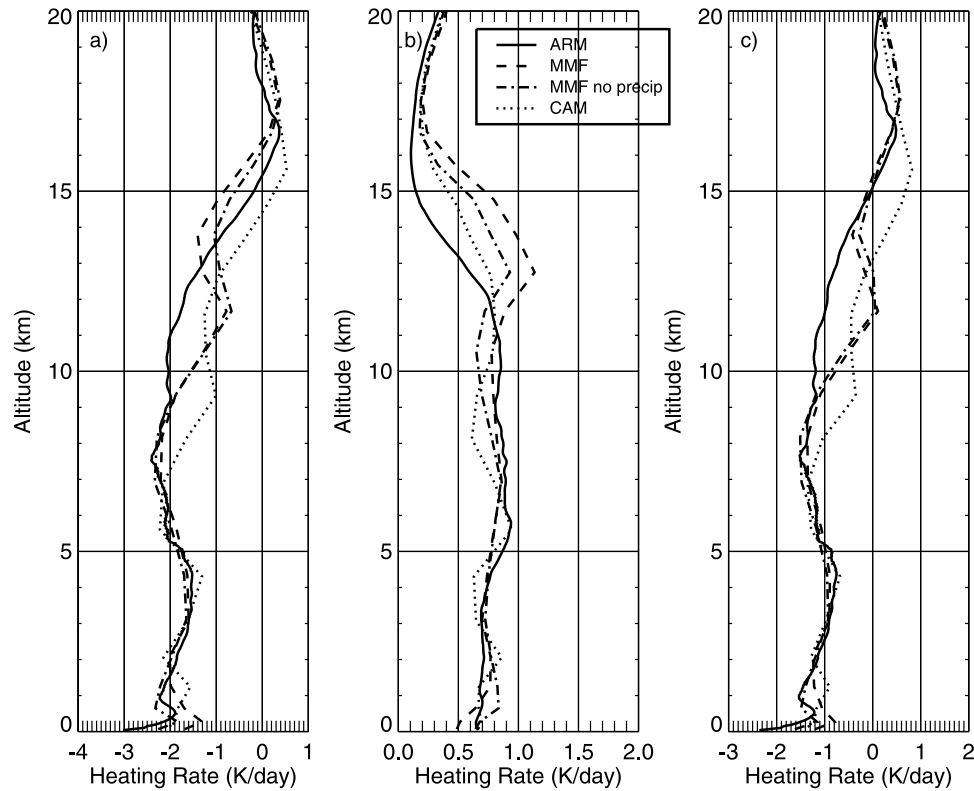


Figure 11. Average (a) longwave, (b) shortwave, and (c) net all-sky heating rate profiles at Manus calculated from ARM observations (solid line), MMF simulation (dashed line), MMF simulation with precipitation removed (dashed-dotted line) and CAM simulation (dotted line).

there is a low-level cloud or clear atmosphere below [Ackerman *et al.*, 1988]. The ARM dataset has more frequent occurrence of mid-level cloud than the CAM or MMF non-precipitating dataset (Figure 2).

[35] In both the CAM and ARM results, the peak LW cooling is at roughly the same height as the peak LW heating and acts to counteract some of the heating in the net LW profile. In the ARM results, this occurs primarily because of the variability in cloud base and top heights seen in the observations. In the CAM, the few optically thick clouds have lower cloud top heights than the optically thin cirrus. In the MMF, peak cooling occurs at a higher altitude than the peak heating, resulting in little cancellation of heating and cooling in the net profiles.

[36] The three datasets have large differences in their ice cloud optical depth distributions (Figure 7). Because radiative transfer processes are a nonlinear function of optical depth, these differences have important impacts on the average heating rates. To illustrate the non-linear effect of ice cloud optical thickness on LW heating rates, we bin the cirrus cases (cloud base > 8 km) in each dataset as a function of IR optical thickness (Figure 14). The magnitude of the maximum LW heating relative to clear sky increases with optical depth, with a very strong increase for $0.1 < \tau < 10.0$. As the optical depth increases, the altitude of the maximum heating tends to decrease. This decrease in altitude occurs both because of changes in cloud base heights and because thicker clouds also tend to have larger CWC values, so the distance from cloud base at which the cloud becomes optically thick decreases. The magnitude of

the maximum cooling rate also increases with increasing optical thickness, although significant cooling does not occur until $\tau > 1.0$. As optical thickness increases beyond 10, the IR emittance approaches 1 and the increase in heating rate tends to flatten out. There are few cirrus clouds with such large optical depths in the current datasets. The similarity in the behavior of the cirrus clouds in the three datasets as a function of ice cloud optical depth indicates that the differences in the average LW heating rates are primarily due to differences in the modeled and observed clouds, not in the treatment of radiative transfer.

[37] Because of the non-linear dependence of heating rate on optical depth, the differences in the net LW heating rate profiles are strongly dependent on the frequency distributions of CWC and optical depth, rather than the mean values. The advantage of the MMF approach is that sub-grid scale variability of in-cloud optical depth is directly included in the calculations. The MMF is able to produce more variability in the CWC and optical depth distributions than the CAM, including large values of in-cloud optical depth that the CAM cannot produce. Correctly simulating the range of variability in the radiative effect of clouds is important in predicting accurate climate sensitivity in a warming atmosphere. The vertical distribution of cloud bases and tops is also important to the radiative heating profiles; as the clouds become optically thick the location of LW heating shifts towards cloud base and LW cooling occurs near cloud top.

[38] The differing effects of ice clouds on the heating rate profiles also leads to significant differences in the level of

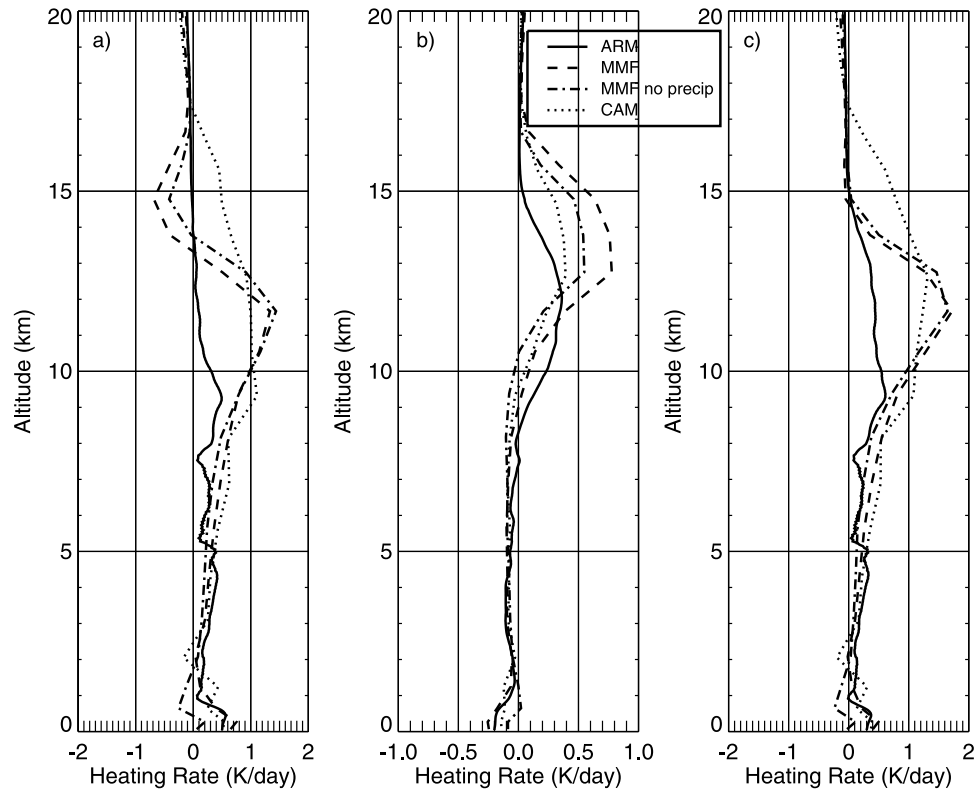


Figure 12. As in Figure 11, but for average all-sky minus clear-sky heating rate profiles, which illustrate the average impact of clouds on the (a) longwave, (b) shortwave, and (c) net heating rate profiles. ARM profiles are indicated by solid line, MMF profiles by dashed line, MMF profiles with precipitation removed by dashed-dotted line, and CAM profiles by dotted line.

Q_0 in the all-sky heating profiles (Figure 11). In the CAM, the LW heating in the ice-cloud layer is reinforced by SW heating in the layer, resulting in large net heating above 14 km. This heating counteracts the cooling due to water vapor, and lowers the average level of Q_0 relative to clear-

sky. In the MMF all-sky profiles, there are two levels of Q_0 . The strong LW heating at the base of the ice cloud layer leads to a level of zero net heating near 12 km. At the top of the ice cloud layer, the strong LW cooling due to ice clouds is almost balanced by the SW heating in the cloud layer,

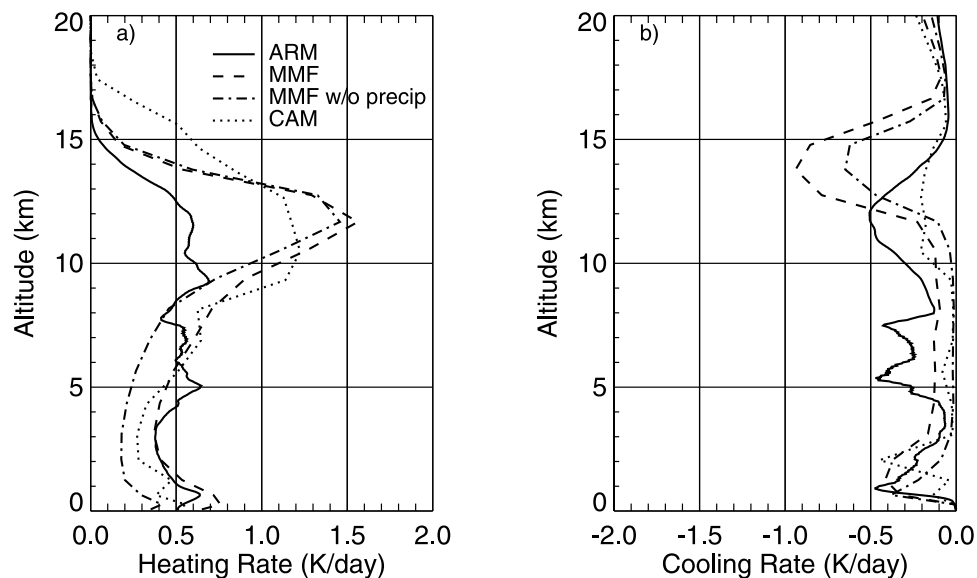


Figure 13. Average longwave (a) heating and (b) cooling rate due to clouds at Manus. Averages are weighted by frequency of heating and cooling at each layer so that sum gives net LW heating rate.

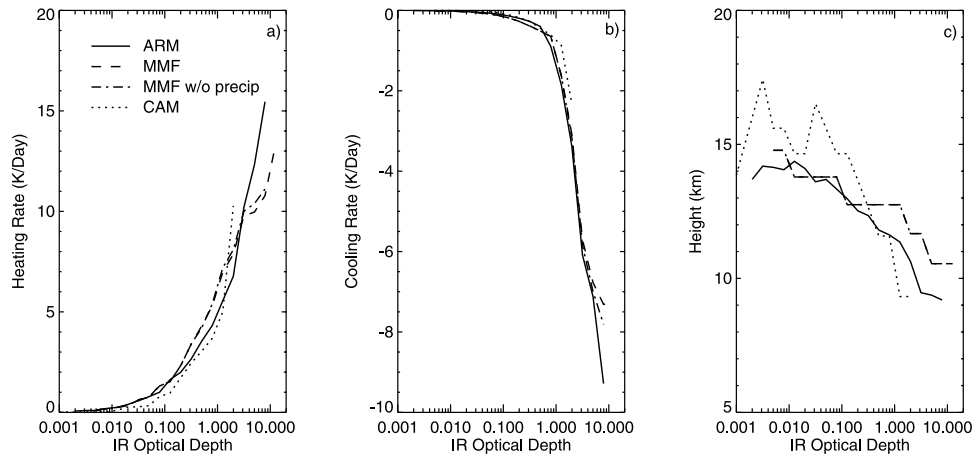


Figure 14. Average (a) heating rate, (b) cooling rate, and (c) altitude of maximum heating rate as a function of IR optical depth for cirrus clouds at Manus. Cirrus clouds are defined as clouds with minimum base height >8 km.

leading to a level of Q_0 close to the clear-sky value. The exact level of Q_0 in the all-sky calculations depends on both the parameterization of the optical properties of the clouds (including effective radius and absorption coefficient) and the frequency of clouds with large optical thickness. Sensitivity calculations by *Gettelman et al.* [2004] indicate that the presence of high cloud will raise the level of Q_0 , with larger increases expected for thicker clouds and for higher cloud tops. The results of this study indicate a more complicated picture in the long term average effects of clouds on the height of the level of Q_0 .

4.3. Clouds and Heating Rates at Nauru

[39] The study period, March through December 1999, was a time of suppressed convection at Nauru [*Mather et al.*, 2007]. Contrasting this period with the more convective period at Manus helps identify robust features in the comparisons between the observations and models. The observations indicated considerably lower frequency of mid-level and high level cloud at Nauru than at Manus (Figure 15). However, the low cloud frequency at Nauru is larger than at Manus, due to the presence of island-induced clouds. During periods of suppressed convection when the prevailing easterlies dominate the large scale flow at Nauru, the diurnal heating of the island surface relative to the ocean can induce frequent local shallow convection that results in cloud trails extending downwind of the island. Due to the location of the ARM site on the downwind side of the island, the ARM observations of low cloud frequency can be overestimated by up to 75% relative to the surrounding ocean [*McFarlane et al.*, 2005].

[40] The models produce significantly less high and mid-level cloudiness at Nauru than at Manus due to the suppressed large scale conditions. As at Manus, over 80% of the CAM ice clouds have tops >15 km. Comparison to the observations of *Comstock et al.* [2002] indicates that the CAM significantly overestimates the frequency of these high clouds at Nauru, while the MMF (21%) and the ARM radar observations (2%) significantly underestimate their frequency. The models produce similar frequency of low level cloud to that observed at the Nauru ARM site

(Figure 15) although the model resolution is too coarse to reproduce the island cloud trail feature. Precipitation is less frequent during the Nauru study period than at Manus and only 2.8% of the radar observations were removed from the dataset due to precipitation. When the precipitating columns (23%) are removed from the MMF dataset, the frequency of boundary layer clouds is greatly reduced while the ice cloud frequency is only slightly reduced. The convection produced by the MMF in this region leads to too much precipitation, but little of the ice cloud is associated with the local convection. The shapes of the frequency distributions of CWC at Nauru (Figure 16) are similar to those at Manus, although with greatly reduced mid-level cloud amounts. The MMF dataset overestimates the frequency

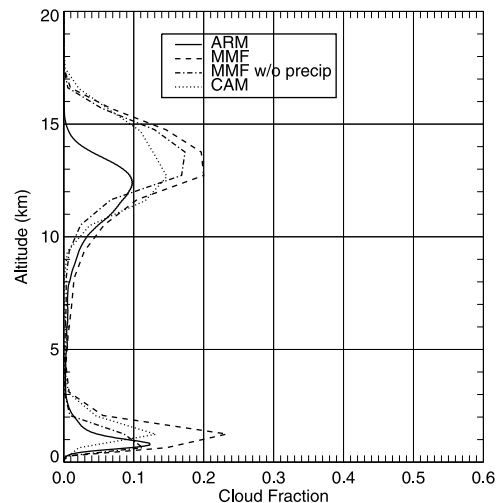


Figure 15. Vertical distribution of average cloud frequency at Nauru from ARM observations (solid line), average cloud frequency of individual CSRM columns in the MMF simulation (dashed line), average cloud frequency from MMF simulation with precipitation removed (dashed-dotted line) and average gridbox cloud fraction from the CAM simulation (dotted line).

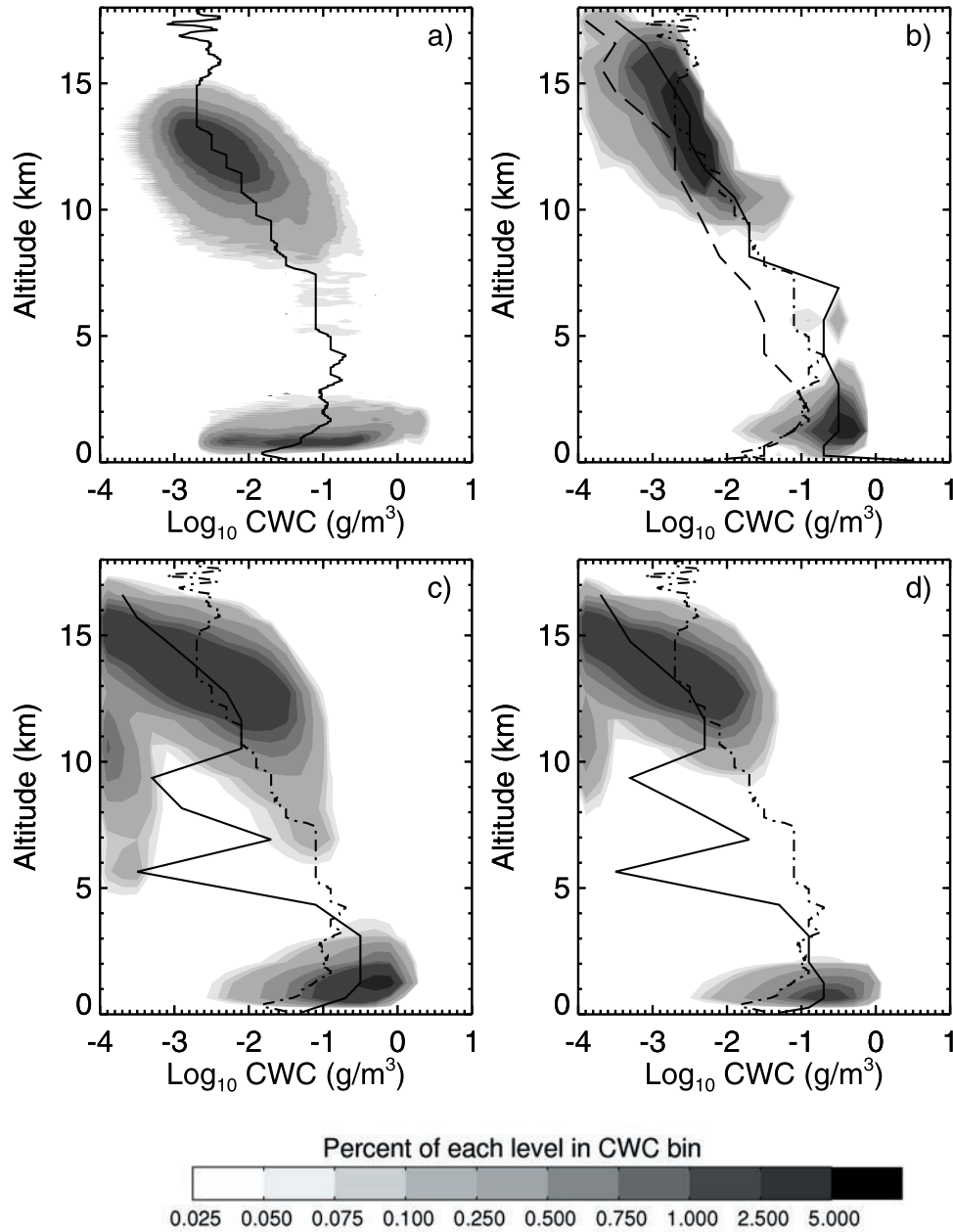


Figure 16. As in Figure 4 but for Nauru.

of very optically thick liquid clouds at Nauru (Figure 17). When the precipitating clouds are removed from the dataset, the liquid cloud optical depth distribution agrees well with the ARM distribution, as does the CAM. The CAM significantly underestimates the in-cloud ice optical depth relative to the ARM observations.

[41] The clear-sky heating rate profiles at Nauru (Figure 18) are very similar to those at Manus although the level of Q_0 is slightly lower at Nauru and the magnitude of the peak LW cooling slightly smaller, due to the lower column water vapor amounts at Nauru. The CAM clear-sky heating rate profiles again show perturbations near 2 km, 5 km and 8 km, which correspond to similar perturbations in the average water vapor profiles (not shown).

[42] The differences in the cloud property distributions at the two sites results in very different average all-sky heating rate profiles at Nauru than at Manus (Figure 19). On average, the effect of low clouds on the heating rate profiles is more pronounced at Nauru and the effect of high clouds less significant than at Manus. The reduced frequency of ice clouds with large optical depth in the MMF and ARM datasets reduces the frequency of profiles with LW cooling. The average LW heating in these datasets extends higher in altitude at Nauru than at Manus, and there is no average LW cooling in the MMF profile. The CAM again has a broad LW heating peak extending to 17 km due to ice clouds, although the magnitude is less than at Manus because of the lower optical depths. The SW profiles show significant

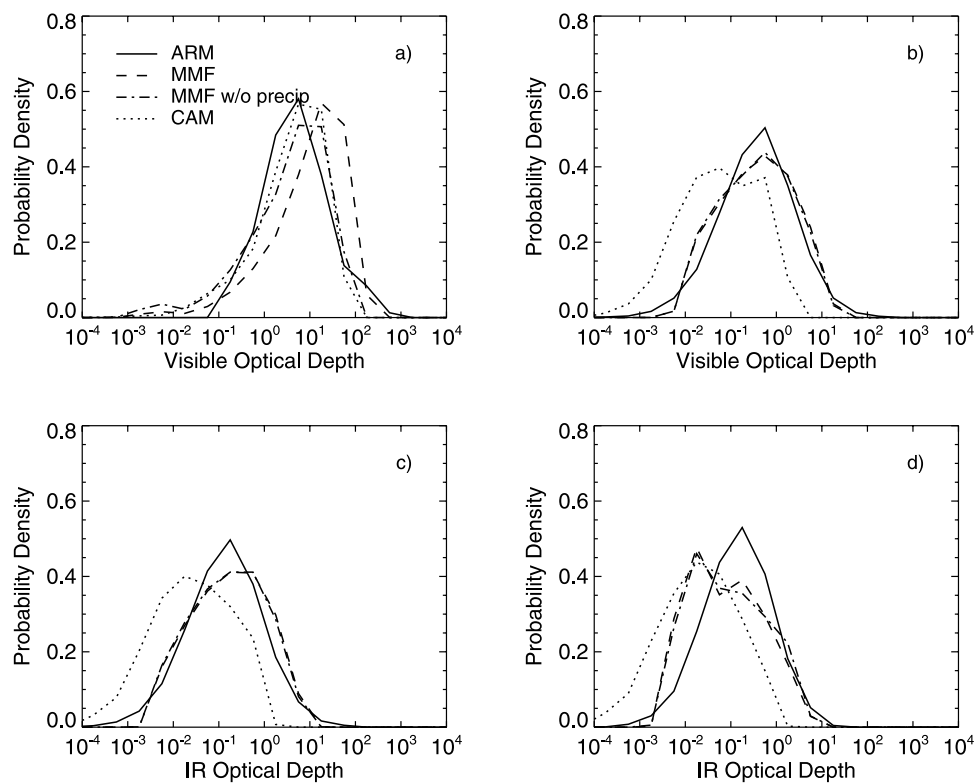


Figure 17. As in Figure 7, but for Nauru.

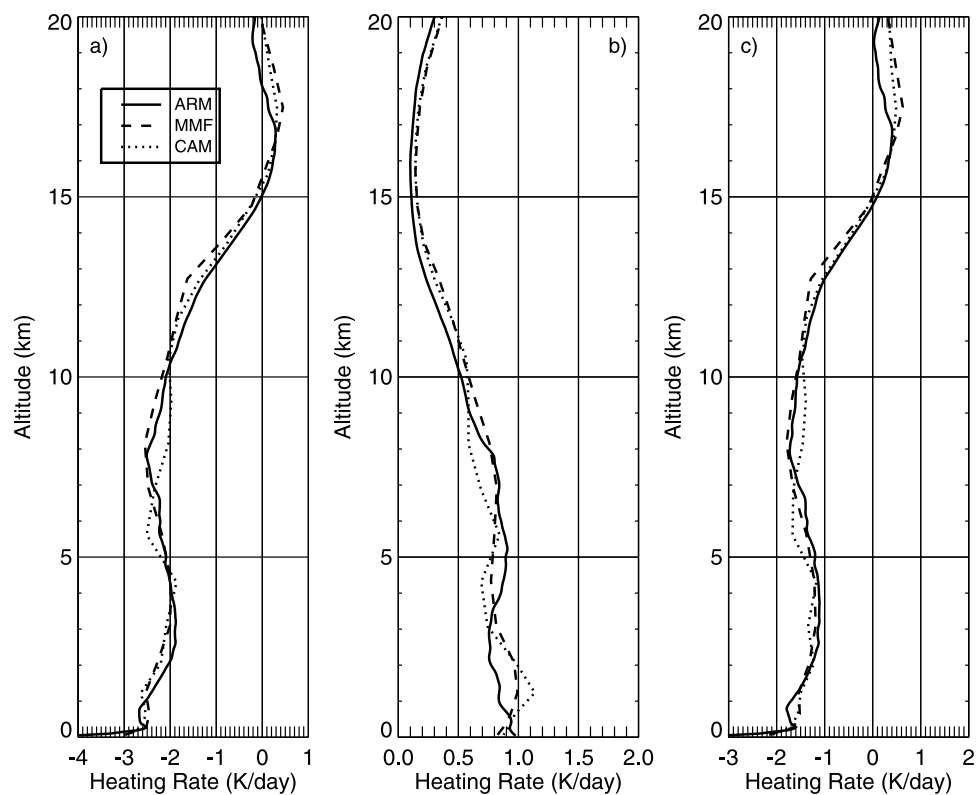


Figure 18. Average calculated clear-sky (a) longwave, (b) shortwave, and (c) net heating rate profiles at Nauru.

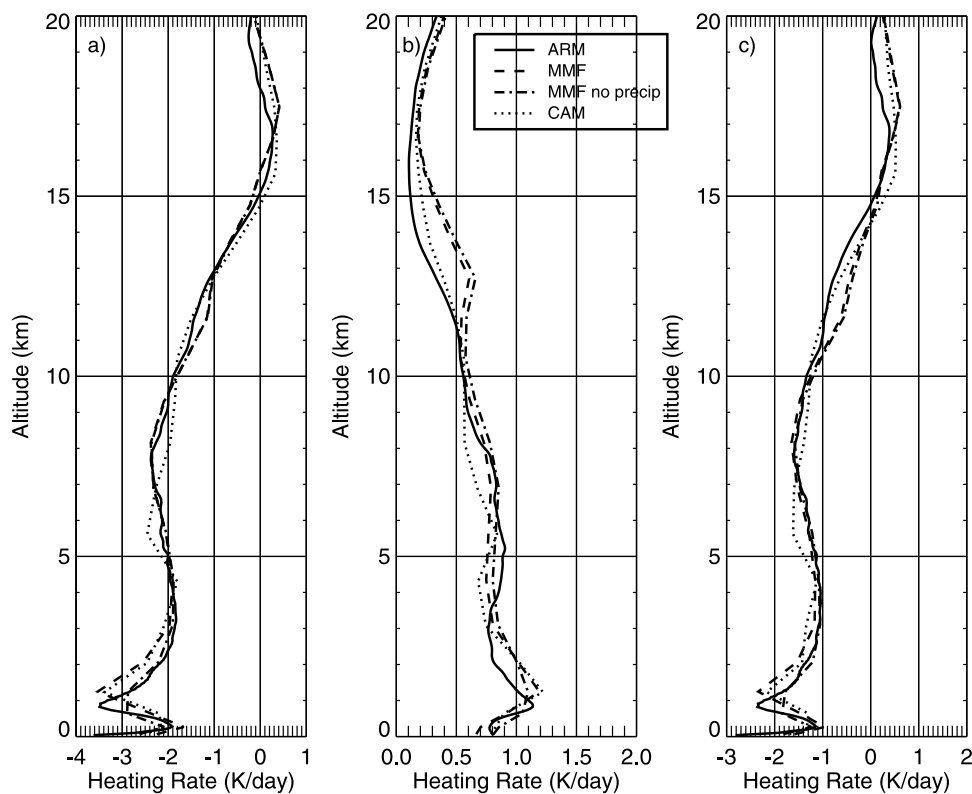


Figure 19. Average calculated all-sky (a) longwave, (b) shortwave, and (c) net heating rate profiles at Nauru.

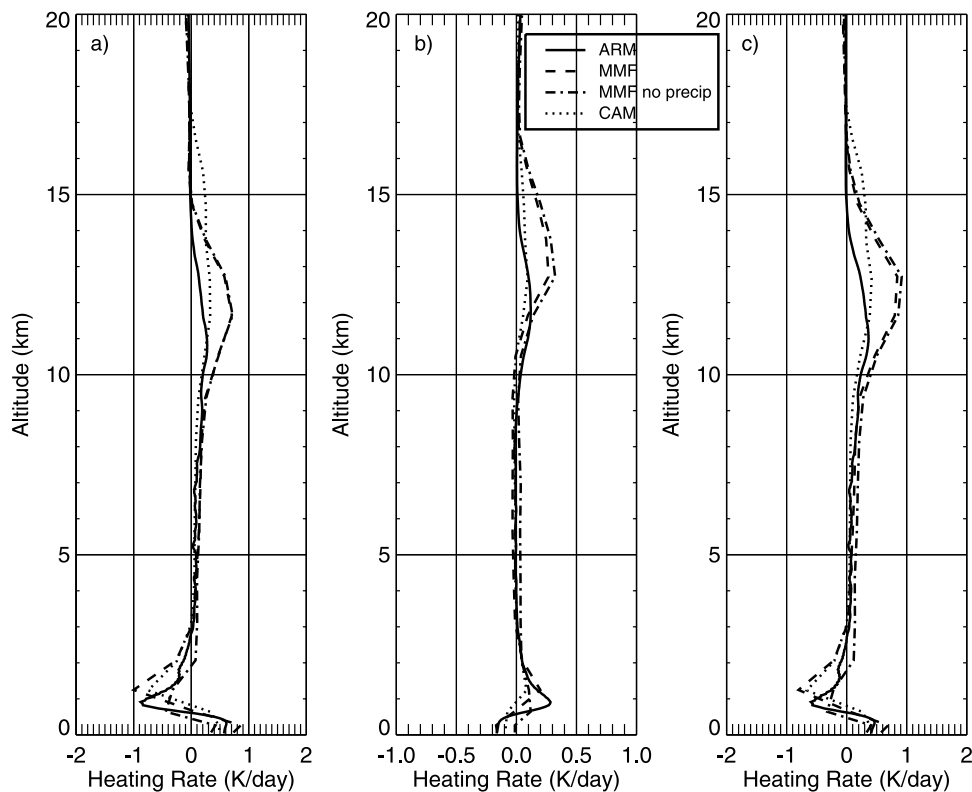


Figure 20. Average calculated all-sky minus clear-sky (a) longwave, (b) shortwave, and (c) net heating rate profiles at Nauru for ARM (solid line), MMF (dashed line), MMF with precipitating columns removed (dashed-dotted line) and CAM (dotted line).

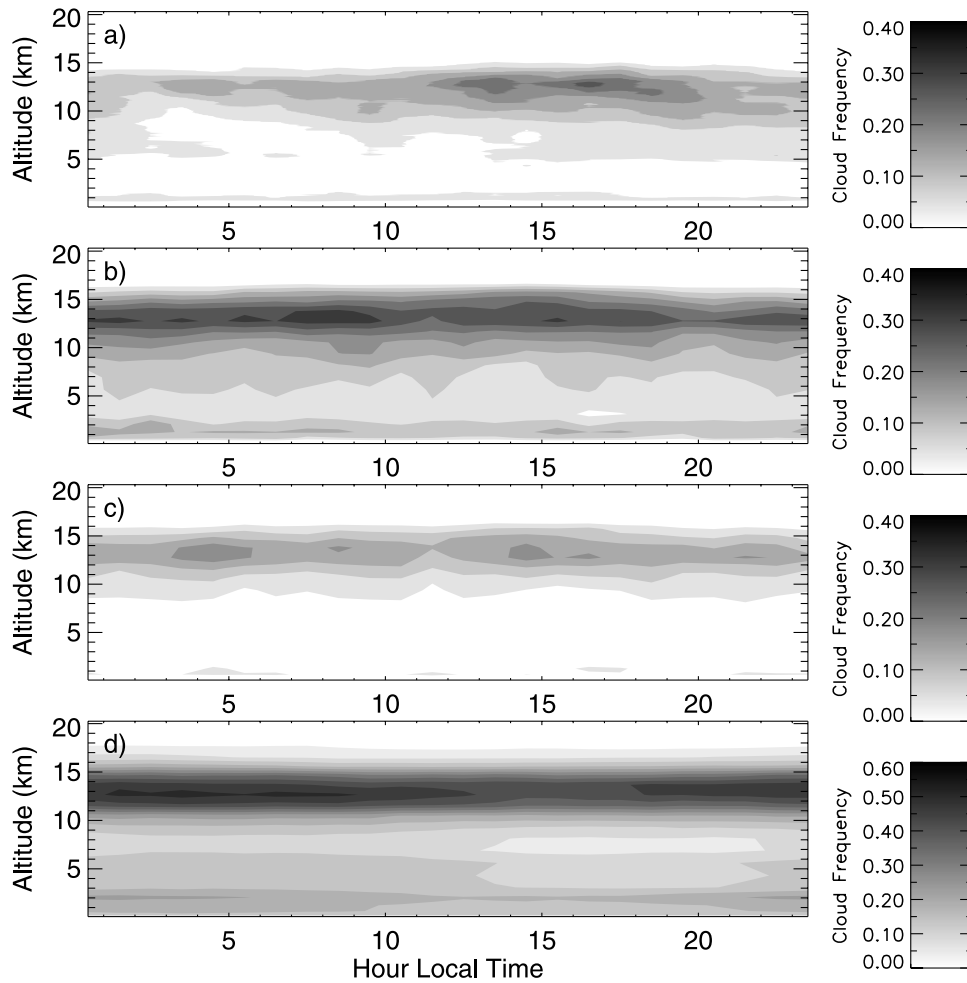


Figure 21. Diurnal composite of average cloud frequency or cloud fraction at Manus for (a) ARM, (b) MMF (with precipitation), (c) MMF (without precipitation) and (d) CAM.

heating in the boundary layer clouds and reduced SW heating in the ice cloud layer relative to Manus. At Nauru, both the MMF and CAM have lower levels of Q_0 in the all-sky profiles than the clear-sky profiles due to the combined LW and SW heating by clouds above 12 km. The level of Q_0 in the CAM profile is not as low as it was at Manus due to the reduced frequency of ice clouds at Nauru. In general, the models and observations show much better agreement in cloud distribution and heating rate profiles under the suppressed conditions of the Nauru period than during the more convectively active period at Manus (Figure 20).

4.4. Diurnal Cycle

[43] In order to investigate the behavior of the climate system in response to non-linear cloud-radiation-climate feedbacks, models need to predict not only the correct average cloud and radiation profiles, but also the correct variability. The diurnal variability of radiative heating is important to dynamics in the tropics. A proposed mechanism for the diurnal cycle of precipitation over the tropical oceans is that radiative heating during the day stabilizes the atmosphere and weakens vertical motions while radiative cooling at night destabilizes the atmosphere, leading to enhanced convection [Xu and Randall, 1995].

[44] The composite diurnal cycle of cloud amount at Manus from the observations and models is shown in Figure 21. The ARM observations show a clear diurnal cycle in ice cloud frequency with increased cloud amount between 1200 and 2000 local time. The MMF simulations show little diurnal variation, while the CAM simulations have a maximum in high cloud amount in the morning. The composite diurnal cycles of net heating due to clouds from the ARM and model calculations show strong variability due to the diurnal variation of incoming SW radiation (Figure 22). The ARM and MMF diurnal profiles show strong heating during the day in the cirrus layer, with cooling at the top of the cirrus layer in the evening and early morning (1800–0700 local time). The ARM results have stronger cooling at night, associated with the diurnal cycle of cloudiness, while the MMF has stronger cooling in the morning. The CAM shows no cooling at night below 18 km, although there is decreased warming from 10 to 15 km relative to the daytime values. This lack of net cooling at night may impact the diurnal cycle in the CAM.

[45] Kubota *et al.* [2004] suggest that cooling at the top of the boundary layer is also an important driver of the diurnal cycle of convection. During the daytime, radiative heating

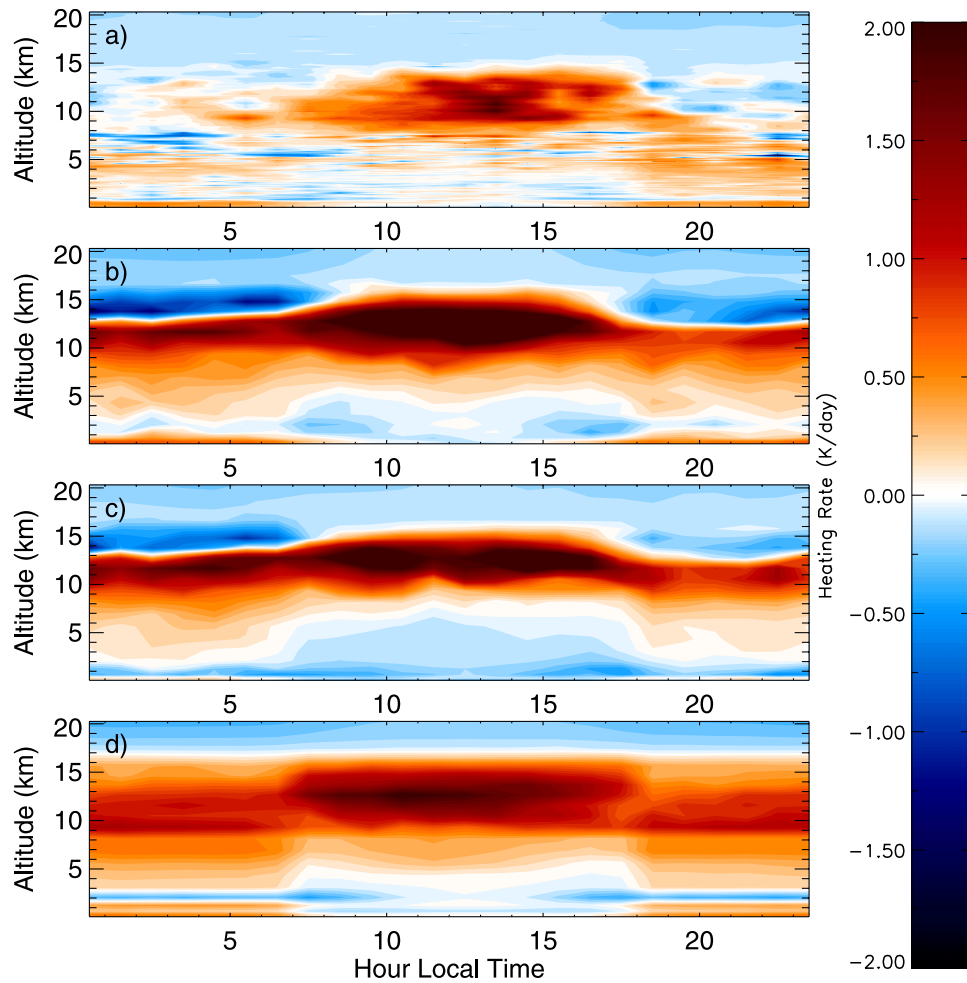


Figure 22. Diurnal composite of net all-sky minus clear-sky heating rate at Manus for (a) ARM, (b) MMF (with precipitation), (c) MMF (without precipitation) and (d) CAM.

at the top of the boundary layer suppresses the growth of convection. At night, destabilization allows moisture transport upward and preconditions the atmosphere for deep convection. The MMF and CAM simulations show stronger and deeper cooling layers above the boundary layer at night than the ARM profiles because the boundary layer clouds in the models extend to higher altitudes than the observed clouds.

5. Conclusions

[46] In a conventional climate model, cloud amount, radiative transfer, and cloud scale dynamics are treated with separate parameterizations, and interact only on the domain-average scale. In the MMF these processes are able to interact at the local cloud-scale. In this study we examined whether the inclusion of sub-grid scale variability of clouds and radiation in the MMF affected the simulation of vertical profiles of cloud properties and radiative heating rates. We found large differences in the vertical profiles of cloud fraction, condensed water content, and cloud effect on heating rates between the models and between the model and observation datasets.

[47] Although the CAM produces a realistic surface energy budget, it has too much high and optically thin ice cloud. The distributions of in-cloud CWC and optical depth of ice clouds in the CAM were significantly narrower than in the observations or MMF results. The small optical depth values in the CAM are due primarily to the large size of the gridbox and lack of subgrid scale variability. Due to the non-linear nature of radiative transfer, the CAM cannot produce the full range of radiative heating responses seen in the ARM results, which has important implications for the climate sensitivity of the model. In particular, due to the low frequency of optically thick ice clouds, the frequency of LW cooling at cloud top is greatly reduced. The lack of optically thick ice clouds and high frequency of optically thin, high altitude ice cloud resulted in a significantly different LW heating distribution in the CAM than in the MMF model. The underestimation of the CAM ice cloud optical depth occurred at both the Manus and Nauru sites. Due to the rarity of deep convection and optically thick ice clouds at the Nauru site, the CAM LW heating profiles were more similar to the MMF and ARM results at Nauru although the CAM still had significant LW heating extending much higher in altitude.

[48] The CAM convective parameterizations produces frequent low-level convection, however significant cloud water is detrained only at a few levels in the model. The CAM has a realistic freezing-level cloud feature resulting from detrained convection, although none of the CAM mid-level clouds contain ice, unlike the ARM observations. The CAM has an unrealistic bimodal boundary layer cloud feature. The top boundary layer cloud peak occurs much higher than the observed boundary layer clouds. Thus strong cloud-top cooling due to low-level clouds occurs too high in the model, which may have implications for the boundary layer dynamics. A striking feature of the CAM diurnal heating rate cycle (Figure 22) is the uniformity of the CAM heating rate profiles relative to the observations. The CAM has very little variability in either the boundary or cirrus layer heating, other than the strong diurnal signal from the SW heating.

[49] Analysis of the surface energy budget indicates that the MMF over-predicts the strength of the effect of clouds on the SW surface fluxes. This is due primarily to the fact that the current version of the MMF has too much active convection in the tropics: it produces precipitation 33% of the time compared to 13% in the observations and overestimates the frequency of occurrence of deep convection and thick cirrus clouds. Analysis of the cause of the MMF overactive tropical convection is underway; preliminary results indicate it may be due to issues with 2D modeling or periodic boundary conditions [Khairoutdinov *et al.*, 2005] or to the effects of 4 km horizontal resolution [Petch and Gray, 2001].

[50] Although the MMF produces too much deep convection, the range of CWC seen in the MMF was more similar to the observations than the CAM. The MMF has a high frequency of optically thick ice clouds, leading to average LW cooling at the top of the ice cloud layer. The frequency of thick ice clouds is too large in the MMF, resulting in overestimation of the magnitude of cooling above 15 km. Although the MMF overestimates the frequency of optically thick clouds, it is able to reproduce the full range of optical thickness and heating rate responses seen in the observations. The MMF also shows stronger diurnal variability in heating rates than the CAM, and is able to partially reproduce the nighttime cooling at the top of the cirrus layer seen in the ARM calculations, which is thought to destabilize the atmosphere and control the diurnal cycle of precipitation.

[51] No mid-level cloud remained in the MMF when precipitating columns were removed. Non-precipitating mid-level cloud in the observations is often shallow altocumulus which may form due to moisture detrained from cumulus congestus that only reach as high as the freezing level. The overly strong convection in the MMF may cause convection to extend too deeply into the atmosphere rather than being inhibited by stability near the freezing level.

[52] The differing frequency of optically thick clouds led to differences in the level of Q_0 in the MMF and CAM at Manus. In the CAM, the presence of high, thin cirrus with no cloud-top cooling raised the level of Q_0 relative to the clear sky value, while in the MMF, the strong LW heating due to ice clouds below 13 km and the combination of LW cooling and SW heating in ice clouds above 13 km led to two levels of Q_0 . At Nauru, where the MMF had consi-

derably less deep convection, the levels of Q_0 in the MMF and CAM were similar and were lower in the all-sky than clear-sky calculations.

[53] Previous studies of the MMF have indicated that it produces a more realistic depiction of tropical precipitation [Ovtchinnikov *et al.*, 2005] and tropical interseasonal variability [Khairoutdinov *et al.*, 2005] than the standard CAM. A recent observational study by Lin *et al.* [2004] indicates that the vertical profile of total diabatic heating may be important to accurate simulation of the MJO. The differing treatments of clouds within the MMF and CAM, including lack of radiation coupling on local scales and interaction of multiple parameterizations within the CAM, produce several important differences in the resulting vertical profiles of cloud and heating rates. In particular, while neither model reproduces all of the characteristics of the observed atmosphere,

[54] (1) The CAM has a significantly larger frequency of thin ice cloud above 15 km than is supported by the observations.

[55] (2) The large size of the CAM gridbox and lack of sub-grid scale variability affects the distribution of in-cloud ice optical thickness in the CAM. The CAM underestimates the variability in cloud properties, and hence in the heating rate profiles.

[56] (3) The differing treatment of cloud and radiation interactions in the two models leads to different vertical profiles of heating in the atmosphere, which may have important impacts on the model dynamics in the boundary layer and upper troposphere.

[57] The exact magnitude of the heating rate differences between the models and ARM results is not a robust feature of the comparisons because it is a function of the parameterization of effective radius, the absorption coefficients used, and the frequency of various cloud types produced in the model simulations. The structure of the vertical distributions of cloud properties in the models is likely affected by their resolution [Inness *et al.*, 2001; Petch and Gray, 2001]. In future work, we will explore the impacts of increasing vertical resolution in both models and increasing horizontal resolution in the MMF. We will also explore the effects of changes in the CAM convective parameterization on the vertical distributions. Zhang and Mu [2005] have examined tropical convection in the CCM3 using the standard Zhang-McFarlane convective parameterization and a revised scheme. The new convective parameterization broadens the precipitation rate distribution (including more heavy precipitation which may be associated with deeper/thicker convective clouds), reduces the upper tropospheric cloud amount, and slightly increases the mid-level cloud amount. In this study, we illustrated that the inclusion of subgrid-scale variability of cloud and radiative processes does have impacts on the vertical profile of radiative heating in the models. In future work we will explore the effect of these heating differences on the local and large-scale dynamics in the models.

[58] **Acknowledgments.** The authors thank Dr. Qiang Fu, Dr. Steve Klein, and an anonymous reviewer for their comments which significantly improved the manuscript. We also thank Annette Koontz for running the CAM and MMF simulations. This work was supported by the U.S. Department of Energy's Office of Biological and Environmental Research as part of the Atmospheric Radiation Measurement Program and by a Grand

Challenge Grant from the Molecular Science Computing Facility (MSCF) in the William R. Wiley Environmental Molecular Sciences Laboratory. The Pacific Northwest National Laboratory is operated by Battelle for the Department of Energy.

References

- Ackerman, T. P., K.-N. Liou, F. P. J. Valero, and L. Pfister (1988), Heating rates in tropical anvils, *J. Atmos. Sci.*, **45**, 1606–1623.
- Bergman, J. W., and H. H. Hendon (1998), Calculating monthly radiative fluxes and heating rates from monthly cloud observations, *J. Atmos. Sci.*, **55**, 3471–3491.
- Blackmon, M., and Coauthors (2001), The Community Climate System Model, *Bull. Am. Meteorol. Soc.*, **82**, 2357–2376.
- Briegleb, B. P. (1992), Delta-eddington approximation for solar radiation in the near community climate model, *J. Geophys. Res.*, **97**, 7603–7612.
- Cahalan, R. F., W. Ridgway, and W. J. Wiscombe (1994), The albedo of fractal stratocumulus clouds, *J. Atmos. Sci.*, **51**, 2434–2455.
- Cole, J. N. S., H. W. Barker, D. A. Randall, M. F. Khairoutdinov, and E. E. Clothiaux (2005), Global consequences of interactions between clouds and radiation at scales unresolved by global climate models, *Geophys. Res. Lett.*, **32**, L06703, doi:10.1029/2005gl020945.
- Collins, W. D. (2001), Parameterization of generalized cloud overlap for radiative calculations in general circulation models, *J. Atmos. Sci.*, **58**, 3224–3242.
- Collins, W. D., et al. (2004), Description of the NCAR Community Atmosphere Model (CAM 3.0, *NCAR Technical Note*, pp. NCAR/TN–464+STR, 226pp.
- Comstock, J. M., T. P. Ackerman, and G. G. Mace (2002), Ground-based lidar and radar remote sensing of tropical cirrus clouds at Nauru Island: Cloud statistics and radiative impacts, *J. Geophys. Res.*, **107**(D23), 4714, doi:10.1029/2002JD002203.
- Cox, S. K., and K. T. Griffith (1979), Estimates of radiative divergence during Phase III of the GARP Atlantic Tropical Experiment: Part II Analysis of Phase III results, *J. Atmos. Sci.*, **36**, 586–601.
- Ebert, E. E., and J. A. Curry (1992), a parameterization of ice-cloud optical-properties for climate models, *J. Geophys. Res.*, **97**, 3831–3836.
- Fu, Q. (1996), An accurate parameterization of the solar radiative properties of cirrus clouds for climate models, *J. Clim.*, **9**, 2058–2082.
- Fu, Q., and K. N. Liou (1992), On the correlated k-distribution method for radiative transfer in nonhomogeneous atmospheres, *J. Atmos. Sci.*, **49**, 2139–2156.
- Fu, Q., and K. N. Liou (1993), Parameterization of the radiative properties of cirrus clouds, *J. Atmos. Sci.*, **50**, 2008–2025.
- Fu, Q., S. K. Kreuger, and K. N. Liou (1995), Interactions of radiation and convection in simulated tropical cloud clusters, *J. Atmos. Sci.*, **52**, 1310–1328.
- Fu, Q., P. Yang, and W. B. Sun (1998), An accurate parameterization of the infrared radiative properties of cirrus clouds for climate models, *J. Clim.*, **11**, 2223–2237.
- Gettelman, A., P. M. de F. Forster, M. Fujiwara, Q. Fu, H. Vomel, L. K. Gohar, C. Johanson, and M. Ammerman (2004), Radiation balance of the tropical tropopause layer, *J. Geophys. Res.*, **109**, D07103, doi:10.1029/2003JD004190.
- Grabowski, W. W. (2001), Coupling cloud processes with the large-scale dynamics using the cloud-resolving convection parameterization (CRCP), *J. Atmos. Sci.*, **68**, 978–997.
- Gray, W. M., and R. W. Jacobsen (1977), Diurnal variation of deep cumulus convection, *Mon. Weather Rev.*, **105**, 1171–1188.
- Hartmann, D. L., and K. Larson (2002), An important constraint on tropical cloud-climate feedback, *Geophys. Res. Lett.*, **29**(20), 1951, doi:10.1029/2002GL015835.
- Hartmann, D. L., J. R. Holton, and Q. Fu (2001), The heat balance of the tropical tropopause, cirrus, and stratospheric dehydration, *Geophys. Res. Lett.*, **28**, 1969–1972.
- Inness, P. M., J. M. Slingo, S. J. Woolnough, R. B. Neale, and V. D. Pope (2001), Organization of tropical convection in a gcm with varying vertical resolution; implications for the simulation of the Madden-Julian Oscillation, *Clim. Dyn.*, **17**, 777–793.
- Ivanova, D., D. L. Mitchell, W. P. Arnott, and M. Poellot (2001), A GCM parameterization for bimodal size spectra and ice mass removal rates in mid-latitude cirrus clouds, *Atmos. Res.*, **59–60**, 89–113.
- Jakob, C., R. Pincus, C. Hannay, and K.-M. Xu (2004), Use of cloud radar observations for model evaluation: A probabilistic approach, *J. Geophys. Res.*, **109**, D03202, doi:10.1029/2003JD003473.
- Johnson, R. H., T. M. Rickenbach, S. A. Rutledge, P. E. Ciesielski, and W. H. Schubert (1999), Trimodal characteristics of tropical convection, *J. Climate*, **12**, 2397–2418.
- Khairoutdinov, M. F., and D. A. Randall (2001), A cloud resolving model as a cloud parameterization in the NCAR Community Climate Model: Preliminary results, *Geophys. Res. Lett.*, **28**, 3617–3620.
- Khairoutdinov, M. F., and D. A. Randall (1997), Cloud resolving modeling of the ARM Summer 19 97 IOP: Model formulation, results, uncertainties, and sensitivities, *J. Atmos. Sci.*, **60**, 607–625.
- Khairoutdinov, M. F., D. A. Randall, and C. DeMott (2005), Simulations of the atmospheric general circulation using a cloud-resolving model as a super-parameterization of physical processes, *J. Atmos. Sci.*, **62**, 2136–2154.
- Kiehl, J. T., and B. P. Briegleb (1991), A new parameterization of the absorptance due to the 15- μ m band system of carbon-dioxide, *J. Geophys. Res.*, **96**, 9013–9019.
- Kiehl, J. T., J. J. Hack, and J. W. Hurrell (1998), The energy budget of the NCAR Community Climate Model: CCM3, *J. Clim.*, **11**, 1151–1178.
- Kristjánsson, J. E., J. M. Edwards, and D. L. Mitchell (2000), Impact of a new scheme for optical properties of ice crystals on climates of two GCMs, *J. Geophys. Res.*, **105**, 10,063–10,079.
- Kubota, H., A. Numaguti, and S. Emori (2004), Numerical experiments examining the mechanism of diurnal variation of tropical convection, *J. Meteorol. Soc. Jpn.*, **82**, 1245–1260.
- Lilly, D. K. (1988), Cirrus outflow dynamics, *J. Atmos. Sci.*, **45**, 1594–1605.
- Lin, J.-L., B. Mapes, M. Zhang, and M. Newman (2004), Stratiform precipitation, vertical heating profiles and the Madden-Julian oscillation, *J. Atmos. Sci.*, **61**, 296–309.
- Lin, W. Y., and M. H. Zhang (2004), Evaluation of clouds and their radiative effects simulated by the NCAR Community Atmospheric Model against satellite observations, *J. Clim.*, **17**, 3302–3318.
- Long, C. N. (2004), The next generation flux analysis: Adding clear-sky LW and LW cloud effects, cloud optical depths, and improved sky cover estimates, in *Fourteenth Atmospheric Radiation Measurement Program Science Team Meeting*, Albuquerque, New Mexico, March 22–26.
- Long, C. N., and T. P. Ackerman (2000), Identification of clear skies from broadband pyranometer measurements and calculation of downwelling shortwave cloud effects, *J. Geophys. Res.*, **105**, 15,609–15,626.
- Mapes, B. E., and P. Zuidema (1996), Radiative-dynamical consequences of dry tongues in the tropical troposphere, *J. Atmos. Sci.*, **53**, 620–638.
- Mather, J. H. (2005), Seasonal variability in clouds and radiation at the Manus ARM site, *J. Clim.*, **18**, 2417–2428.
- Mather, J. H., T. P. Ackerman, W. E. Clements, F. J. Barnes, M. D. Ivey, L. D. Hatfield, and R. M. Reynolds (1998), An atmospheric radiation and cloud station in the Tropical Western Pacific, *Bull. Am. Meteorol. Soc.*, **79**, 627–642.
- Mather, J. H., S. A. McFarlane, M. A. Miller, and K. L. Johnson (2007), Cloud properties and associated heating rates in the tropical western Pacific, *J. Geophys. Res.*, **112**, D05201, doi:10.1029/2006JD007555.
- McFarlane, S. A., C. N. Long, and D. M. Flynn (2005), Impact of island-induced clouds on surface measurements: Analysis of the ARM Nauru island effect study data, *J. Appl. Meteorol.*, **44**, 1045–1065.
- Ovtchinnikov, M., T. P. Ackerman, R. Marchand, and M. Khairoutdinov (2005), Evaluation of the multi-scale modeling framework using data from the Atmospheric Radiation Measurement program, *Submitted to J. Clim.*
- Petch, J. C., and M. E. B. Gray (2001), Sensitivity studies using a cloud-resolving model simulation of the tropical west pacific, *Q. J. R. Meteorol. Soc.*
- Randall, D., M. Khairoutdinov, A. Arakawa, and W. Grabowski (2003), Breaking the cloud parameterizations deadlock, *Bull. Am. Meteorol. Soc.*, **84**, 1547–1564.
- Raymond, D. J. (2000), The Hadley circulation as a radiative-convective instability, *J. Atmos. Sci.*, **57**, 1286–1297.
- Slingo, A. (1989), A GCM parameterization for the shortwave radiative properties of water clouds, *J. Atmos. Sci.*, **46**, 1419–1427.
- Slingo, A., and J. M. Slingo (1988), The response of a general circulation model to cloud longwave radiative forcing. I: Introduction and initial experiments, *Q. J. R. Meteorol. Soc.*, **114**, 1027–1062.
- Smirnov, A., B. N. Holben, Y. J. Kaufman, O. Dubovik, T. F. Eck, I. Slutsker, C. Pietras, and R. N. Halthore (2002), Optical properties of atmospheric aerosol in maritime environments, *J. Atmos. Sci.*, **59**, 501–523.
- Stephens, G. L., and P. J. Webster (1981), Clouds and climate - sensitivity of simple systems, *J. Atmos. Sci.*, **38**, 235–247.
- Tao, W.-K., S. Lang, J. Simpson, C.-H. Sui, B. Ferrier, and M.-D. Chou (1996), Mechanisms of cloud-radiation interaction in the tropics and midlatitudes, *J. Atmos. Sci.*, **53**, 2624–2651.
- Xu, K.-M., and D. A. Randall (1995), Impact of interactive radiative transfer on the macroscopic behavior of cumulus ensembles. Part II: Mechanisms for cloud-radiation interactions, *J. Atmos. Sci.*, **52**, 800–817.
- Zhang, C., and M.-D. Chou (1999), Variability of water vapor, infrared radiative cooling, and atmospheric instability for deep convection in the equatorial western Pacific, *J. Atmos. Sci.*, **56**, 711–723.
- Zhang, G. J., and M. Mu (2005), Effects of modification to the Zhang-McFarlane convection parameterization on the simulation of the tropical

- precipitation in the National Center for Atmospheric Research Community Climate Model, version 3, *J. Geophys. Res.*, *110*, D09109, doi:10.1029/2004JD005617.
- Zhang, Y. C., W. B. Rossow, A. A. Lacis, V. Oinas, and M. I. Mishchenko (2004), Calculation of radiative fluxes from the surface to top of atmosphere based on ISCCP and other global data sets: Refinements of the radiative transfer model and the input data, *J. Geophys. Res.*, *109*, D19105, doi:10.1029/2003JD004457.
- Zuidema, P. (1998), The 600–800 mb minimum in tropical cloudiness observed during TOGA-COARE, *J. Atmos. Sci.*, *55*, 2220–2228.
-
- T. P. Ackerman, Joint Institute for the Study of the Atmosphere and Ocean and Department of Atmospheric Sciences, University of Washington, Seattle, Washington, USA.
- J. H. Mather and S. A. McFarlane, Climate Physics Group, Pacific Northwest National Laboratory, P.O. Box 999, MS K9-24, Richland, WA 99352, USA. (sally.mcfarlane@pnl.gov)